

Fine-tuning neural-operator architectures for training and generalization

Jose Antonio Lara Benitez^{1,a,*}, Takashi Furuya^{2,b,*}, Florian Faucher³, Xavier Tricoche⁴, and Maarten V. de Hoop¹

¹Rice University

²Shimane University

³Team Makutu, Inria Bordeaux, University of Pau and Pays de l'Adour.

⁴Purdue University

^aEmail: antonio.lara@rice.edu

^bEmail: takashi.furuya0101@gmail.com

*These two authors contributed equally to this work

Abstract

In this work, we present an analysis of the generalization of Neural Operators (NOs) and derived architectures. We proposed a family of networks, which we name ($sNO + \varepsilon$), where we modify the layout of NOs towards an architecture resembling a Transformer; mainly, we substitute the Attention module with the Integral Operator part of NOs. The resulting network preserves universality, has a better generalization to unseen data, and similar number of parameters as NOs. On the one hand, we study numerically the generalization by gradually transforming NOs into $sNO + \varepsilon$ and verifying a reduction of the test loss considering a time-harmonic wave dataset with different frequencies. We perform the following changes in NOs: (a) we split the Integral Operator (non-local) and the (local) feed-forward network (MLP) into different layers, generating a "sequential" structure which we call sequential Neural Operator (sNO), (b) we add the skip connection, and layer normalization in sNO , and (c) we incorporate dropout and stochastic depth that allows us to generate deep networks. In each case, we observe a decrease in the test loss in a wide variety of initialization, indicating that our changes outperform the NO. On the other hand, building on infinite-dimensional Statistics, and in particular the Dudley's Theorem, we provide bounds of the Rademacher complexity of NOs and sNO , and we find the following relationship: the upper bound of the Rademacher complexity of the sNO is a lower-bound of the NOs, thereby, the generalization error bound of sNO is smaller than NO, which further strengthens our numerical results.

1 Introduction

Data-driven approximations of Operators among functional spaces are gaining momentum. It provides an efficient way to evaluate models over costly PDEs solvers for parametric families of PDEs, whenever the constitutive laws are already known, or the laws are approximated, or only the data is presented. Once the model is fully-trained, the solution is, up to an approximation error, equivalent to the forward evaluation of the neural network, upon assumptions in the input's distribution (that the test data come from the same, or perhaps *close enough*, distribution as the training). While several methods have been studied in the last years, such as DeepONets [Lu et al., 2021, 2022], PCA-Net [Bhattacharya et al., 2021, Hesthaven and Ubbiali, 2018], and PINNs [Karniadakis et al., 2021, Raissi et al., 2019], Neural Operators (NOs) [Kovachki et al., 2021b, Li et al., 2020a,b], with a special mention to the Fourier Neural Operators (FNOs), are widely used as one of the main Operator Learning tools, as they present interesting properties: (a) the

costly Integral Operator is implementable, (b) the network presents the so-called discretization invariant attribute¹, (c) provably universality; upon regularity and separability of spaces. Hence, NOs or iterations thereof, [Brandstetter et al., 2022, Tripura and Chakraborty, 2022, Wen et al., 2022a], rapidly become the choice network for Operator Learning; finding application in multiple scientific domains [Grady II et al., 2022, Guan et al., 2021, Kurth et al., 2022, Li et al., 2022a, Pathak et al., 2022, Wen et al., 2022b, Yin et al., 2022]. Although FNOs result in state-of-the-art performance in solving certain parametric PDEs, for instance, *Incompressible Navier-Stokes Equations*, see Kovachki et al. [2021a, Section 3.2], still it has not been fully tested in more realistic 3D large-scale PDEs problems [Li et al., 2022b] and has been partially tested with non-linear inverse problems [Yang et al., 2021]. Depending on the applications, some maps are hard to approximate without increasing the capacity of the network, and in doing so, some issues appear such as overfitting and stability of the training. In particular, NOs are the natural generalization of MLPs on functional spaces, and thus, problems of the latter remain in the former. For instance, You et al. [2022] observed for FNOs that deep architectures do not efficiently approximate non-linear operators for PDEs, despite being universal [Kovachki et al., 2021a]. Hence, adjustments are needed to allow architecture families with more *desirable* properties.

At the same time, seemingly different architectures: Transformers, [Devlin et al., 2018, Dosovitskiy et al., 2020, Vaswani et al., 2017], have established as the dominant backbone in deep learning; replacing Long Short-Term Memory (LSTM) in NLP task, and superseding Convolutional Neural Nets (ConvNets), while not being limited to image classification [Liu et al., 2021]. In Kovachki et al. [2021b, Section 3.3], the authors find Neural Operators and Transformers are connected; Attention can be interpreted as a Monte-Carlo approximation of a *Nonlinear Integral Operator*. This has been independently explored in Cao [2021], Kissas et al. [2022], where Attention is incorporated in the network design. One of the main principles driving the success of Transformers is their excellent ability to capture the long-range, or global, information, either in sequences or images [Khan et al., 2021], a property known as *the non-local behavior*. However, Neural Operators have already incorporated this at a fraction of the computational cost: for FNOs or Wavelet-based NO. That is, while Attention is an operation with cost $\mathcal{O}(n^2)$ on input size; making it prohibitively expensive for large inputs, the *Convolutional Integral Operator* in FNOs is efficiently estimated by the Fast Fourier Transform (FFT), with a computational cost of $\mathcal{O}(n \log n)$. In spite of this fact, some ideas like shifted windows have been incorporated in (visual) Transformers to overcome this issue, but without solid theoretical ground.

There exists overwhelming evidence that design choices in Transformers improve the capacity of the deep neural network, and makes it more stable under training; for instance, the return of ConvNets [Liu et al., 2022] in image task is possible by "*modernizing*" a standard ResNet toward the design of a vision Transformer. Therefore, it is natural to ask if likewise, we can observe some of the benefits in Neural Operators. Abstracting the layout of the Transformer has been previously expressed in different domains: in vision, and language, see Yu et al. [2022], and particularly in Lee-Thorp et al. [2021]. Although, the previous references are not stated in functional space as we presented here.

Our Contributions

- (a) We modify Neural Operators by choosing design ideas presented in Liu et al. [2022]. We refer to the resulting architecture as $(sFNO + \varepsilon)$ and $(sNO + \varepsilon)$, respectively for experiments and theory; where the ε indicates that minor changes are incorporated in the main network.
- (b) Considering wave propagation datasets, we experimentally observe that modifying FNOs towards $(sFNO + \varepsilon)$ leads to a smaller test loss, which raises the question if the improvement can be proven by theory (next points).

¹In the sense of zero-shot superresolution.

- (c) In the process, we gradually modify the architecture to understand the empirical impact of the design changes. After multiple random initializations, we analyze the test loss. Showing that our findings are consistent among multiple realizations of the training path and initialization(s) of the networks.
- (d) Building on the tools in Li et al. [2018a] we provide a visualization of the loss landscapes of FNOs, ($s\text{FNO} + \varepsilon$), and the architectures in between.
- (e) Using the tools in Giné and Nickl [2015], Wainwright [2019] we provide an analysis of the generalization error bound of general Neural Operators, whose non-local operator is defined by the linear integral operator, and not based on discretization and estimation of convolutional integral operator by the FFT algorithm. That is, our analysis is general in the sense that it applies independently of the discretization and the choice of the basis expansion² in integral operators. Moreover, our work not only generalizes results of Kim and Kang [2022], but also provides a better bound of the Rademacher complexity with order $\mathcal{O}(1/n^{\frac{1}{\hat{d}+1}})$ (n is the number of training data and \hat{d} is the doubling number of $D \times D$, where D is the spatial domain), whilst $\mathcal{O}(1)$ in Kim and Kang [2022].
- (f) We also present an analysis of the generalization error bound of a *simplified version* of the proposed architecture, named hereinafter as sequential structure or $s\text{NO}$. We prove a reduction of the bound in the generalization error, which boils down to a solid theoretical foundation of our experimental results.

We expect the ideas in this paper may influence the evolution of Neural Operators towards architectures with more desirable properties, for instance, by preserving universality and reducing the test loss with the same parameter size as (traditional) Neural Operator counterparts.

2 Proposed method

Inspired by the return of ConvNets [Liu et al., 2022], the connection of Neural Operators with Transformers [Kovachki et al., 2021b, Section 5.2], and the abstraction of the Token Mixer [Yu et al., 2022], we propose a “modernization” of NOs with our architecture ($s\text{NO} + \varepsilon$). To understand which changes are most important, we gradually modify the NOs until obtaining ($s\text{NO} + \varepsilon$). In each step, we aim to support the numerical evidence with theoretical reasoning. Particularly, we prove that the upper bound of “sequential” structure of the ($s\text{NO} + \varepsilon$) is a lower bound of the corresponding bound for the NO without losing approximation properties (i.e. it is still a universal approximator). Therefore, we provide theoretical and numerical steps explaining the success of ($s\text{NO} + \varepsilon$), and the empirical observations of Yu et al. [2022].

2.1 Neural Operator: Standard structure

We briefly review the standard (additive) Neural Operator introduced by Kovachki et al. [2021a,b]. Let \mathcal{K}_ℓ be the Linear Integral Operator (non-local), see Definition A.3 in Appendix A.3, and W_ℓ be the weight matrix (local). The standard structure is then defined as

$$v_{\ell+1} = \sigma \circ (W_\ell + \mathcal{K}_\ell + b_\ell) \circ v_\ell, \quad (1)$$

($\ell = 1, \dots, L$) where σ is an elementwise nonlinear activation function, and b_ℓ is a bias. $v_1 = \mathcal{R}(a)$, i.e., the parameter a is lifted by the map \mathcal{R} , and finally, the output is projected back to the corresponding space by \mathcal{Q} , forming the solution field $u = \mathcal{Q}(v_{L+1})$. We refer to Appendix A.4 for details.

²In particular, Fourier basis corresponding to FNOs.

2.2 Sequential structure

One of the prominent changes in MetaFormers and Transformers [Vaswani et al., 2017, Yu et al., 2022], is the compositional structure of the non-local and local layers, instead of adding the operations within the same layer. Namely, the Mixing Token (Attention, Pooling, etc.) precedes a traditional MLP acting on the channels or feature space; see Figure 1. This structure is close to the one described by Kovachki et al. [2021a, Section 2.5.1] for 1-layer NN and FNOs; in this work is observed that universality is preserved, the result can be expanded to a more general MLP architecture with M th-layer.

We introduce the sequential Neural Operator (s NO). Let f_ℓ be a MLP with M th-layer (local), Goodfellow et al. [2016, Ch. 6]. The sequential structure is then defined as

$$\begin{aligned} w'_\ell &= \sigma \circ (\mathcal{K}_\ell + b_\ell) \circ v_\ell, & (\text{Non-local}) \\ v_{\ell+1} &= f_\ell \circ w'_\ell, & (\text{Local}) \end{aligned}$$

($\ell = 1, \dots, L$). For a visual representation of the architecture, see Figure 1.

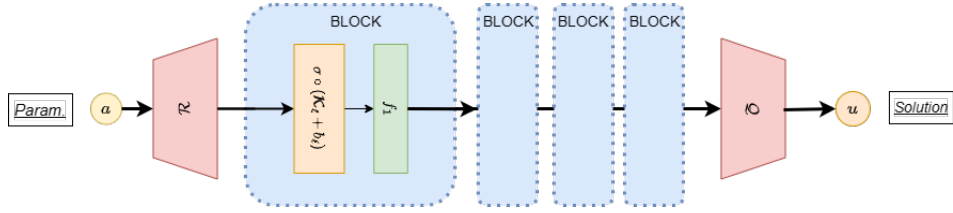


Figure 1: **sNO**. It is a general architecture abstracted by merging the sequential structure presented in Transformers/Meta Formers by setting the Integral Operator in the Token Mixer, and separating it from the local part. For comparison with the NO, see Figure 6.

If a convolutional Integral Operator is chosen for \mathcal{K} , we find a significant improvement over the relative L^2 -norm compared to traditional FNOs, for the same parameter budget, see Figure 4 for comparison. Theoretically, the observed results follow immediately from Corollary 4.9.

2.2.1 Remark: Universality

Kovachki et al. [2021b, Theorem 11] have shown that the compositional operator $(\sigma \circ \mathcal{K}_L) \circ \dots \circ (\sigma \circ \mathcal{K}_1)$ of the Linear Integral Operator \mathcal{K}_ℓ and the elementwise nonlinear activation function σ , can approximate any nonlinear continuous operator, thus, any local operation in Neural Operators does not affect the Universality property, i.e., standard and sequential structures have the universality property.

2.3 (s NO + ε) version 1

Prevalent in modern NNs architectures is the presence of the skip connection, which we incorporate together with a layer normalization in the previous structure. The architecture can be understood as an instance of the MetaFormer in Yu et al. [2022]; whence, the Token Mixer is substituted by an Integral Operator, and the Network is extended to functional space (this is not done in the above-mentioned paper). Using a similar notation, we have

$$w'_\ell = (\mathbf{I}_d + \sigma \circ (\mathcal{K}_\ell + b_\ell) \circ N) \circ v_\ell, \quad (3a)$$

$$v_{\ell+1} = (\mathbf{I}_d + f_\ell \circ N) \circ w'_\ell, \quad (3b)$$

($\ell = 1, \dots, L$) where \mathbf{I}_d is the Identity operator, and N is the layer normalization (or any other normalization). See Figure 2.

If the Integral Operator is convolutional (as in FNOs), and estimated by the FFT algorithm, the architecture has similarities with FNet [Lee-Thorp et al., 2021]. These connections have not been explored in the

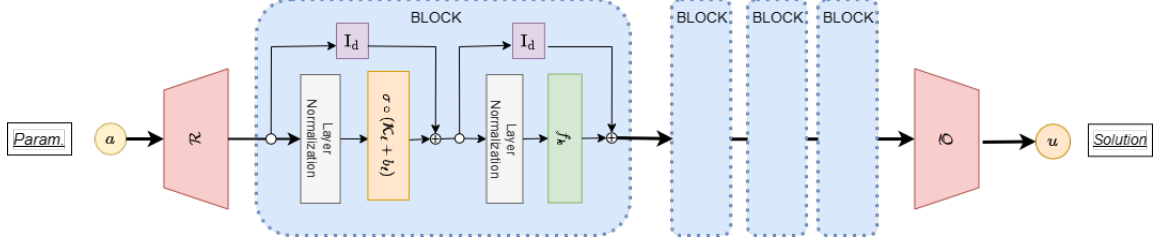


Figure 2: **(sNO + ε) version 1**. It is a modification based on the sequential structure in where we incorporate layer normalization and skip connection as in modern Transformers. For comparison with the NO, see Figure 6.

previous work with respect to Operators defined through PDEs, see Appendix A.9. In previous work, You et al. [2022] incorporate the skip connection into a (Fourier) Neural Operator block, however, the previously described sequential structure is not presented. Furthermore, similarities with You et al. [2022] are possible, that is, the skip connection can be interpreted as unrolling the Newton’s method. We refer to Appendix A.9 for details.

Comparing (sNO + ε)v1 with NOs and sNOs, we find an improvement over the test set in multiple settings. Besides, it should be noticed from Figure 4 that the skip connection has an impact on the loss-landscape, the local minima find by the optimization algorithm are alike, i.e., a consistent value of the loss function on test data through multiples trained networks.

2.4 (sNO + ε) version 2

Ultimately, we incorporate dropout [Srivastava et al., 2014], and to increase the capacity of the Network, without suffering overfitting, we incorporate stochastic depth, [Huang et al., 2016]. That is,

$$w'_\ell = (\mathbf{I}_d + \sigma \circ (\mathcal{K}_\ell + b_\ell) \circ \mathbf{N}) \circ v_\ell, \quad (4a)$$

$$v_{\ell+1} = (\mathbf{I}_d + \mathbf{X} f_\ell \circ \mathbf{N}) \circ w'_\ell, \quad (4b)$$

($\ell = 1, \dots, L$) where \mathbf{X} is a Bernoulli RV³, $\mathbf{P}\{\mathbf{X} = 1\} = p_\ell$, and $\mathbf{P}\{\mathbf{X} = 0\} = 1 - p_\ell$ for $p_\ell \in [0, 1]$, likewise \mathbf{N} is the layer normalization (or any other normalization). This has been previously used in Swin Transformers, [Liu et al., 2021], and ConvNeXt [Liu et al., 2022], among other architectures, with relative success in training very deep neural networks, avoiding some of the usual issues associated with depth. Lastly, following Liu et al. [2022], the epochs in the training are extended.

3 Experiments

3.1 Wave dataset

The architectures, as well as all the intermediate steps leading to (sFNO + ε), are tested with a dataset corresponding to the propagation of acoustic waves in two-dimensional domain. We consider the propagation of time-harmonic waves described by the Helmholtz equation, see Appendix B. The propagation is given in terms of pressure field p that solves a partial differential equation (PDE) which depends on the wave speed c that characterizes the medium. Therefore, our dataset consists of the couples (c, p) where p solves the acoustic wave equation with wave speed c . We refer to Appendix B for the precise steps to generate the data. Then, the objective of the network (after training) is, given an input wave speed model c , to predict the pressure field p that represents the propagation of acoustic waves.

³RV refers to Random Variable.

3.2 Reconstruction results

The choice of hyperparameters and thorough analysis of the performance of the architectures for our dataset corresponding to wave propagation are given in Appendix C. For the experiments, we work with convolutional Integral Operators estimated by the FFT. However, our proofs are stated in full generality for NO, and sNO.

The reconstructions of the wave fields using the different architectures are pictured in Figure 3, together with the relative error with the reference solution obtained from the discretization of the wave PDE, see Appendix B. The comparison of the test-loss for the different architectures is shown Figure 4.

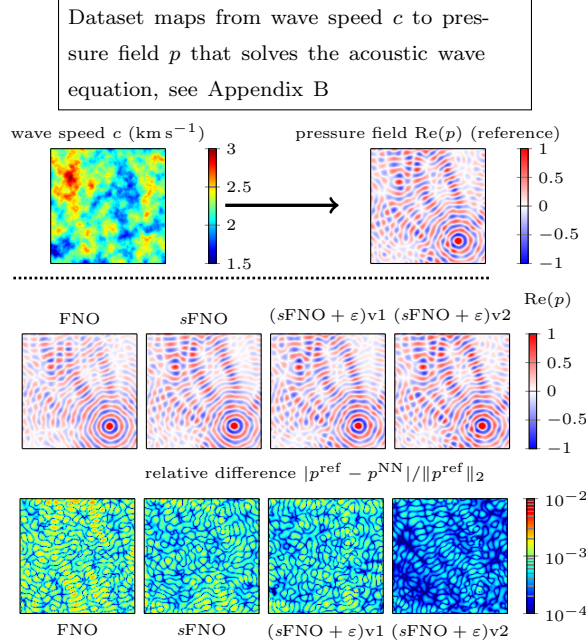


Figure 3: Comparison of the reconstructed wavefields obtained with the different architectures (middle row) and relative error with the reference solution (bottom row). The dataset corresponds to wave propagation from Gaussian Random Field realizations of wave speed in a domain of size $3.81 \times 3.81 \text{ km}^2$, with reference wavefield obtained by solving the wave PDEs with software **hawen** [Faucher, 2021] (top row). This configuration corresponds to Experiment 1 of Appendix B where additional realizations are provided.

We see that FNO architecture has arguably the *worst* behaviour in terms of test loss value, also in the field reconstruction, see Figures 3 and 4. There is a noticeable improvement when the sequential structure is incorporated (sFNO). Furthermore, adding the skip connection improves over the previous results: (sFNO + ϵ) version 1, and (sFNO + ϵ) version 2. Particularly, version 2 allows us to have a very deep NN leading to the best reconstruction. These changes significantly increase the capacity of the neural network, without overfitting. Besides, We notice that (sFNO + ϵ) in any version, yields better and more concentrated testing results, i.e., the variance of the test-loss is significantly reduced whenever the skip connection is added, cf. Figure 4.

3.3 Visualization of the loss landscape

To further strengthen the previous numerical experiments, we implement the algorithm described in Li et al. [2018a], allowing for a side-by-side comparison between loss functions across architectures. From Figure 5, it can be seen that sNO and sFNO + ϵ present flatter landscapes in the PCA directions compared with FNO. In fact, the flatter the loss-landscape, the smaller the generalization error, see Figure 4. We refer to the Appendix C.3 for a full description of the procedure.

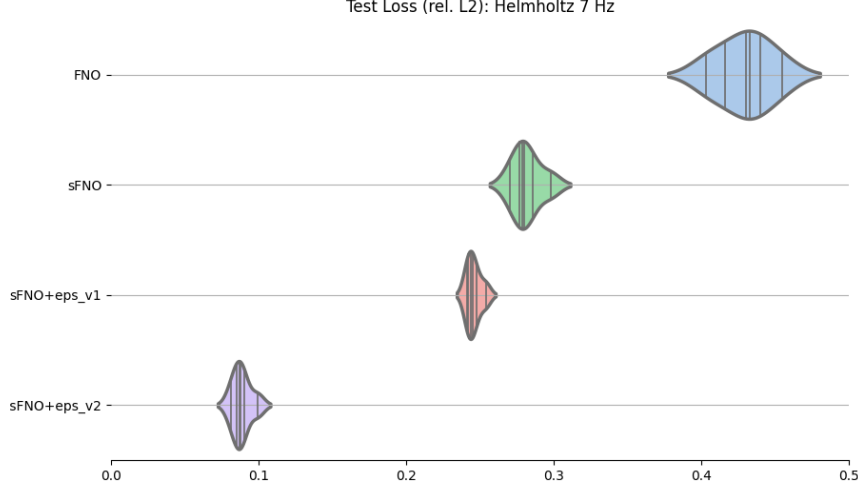


Figure 4: **Comparison of test-loss for the Experiment 1 of Appendix B.** Each architecture is trained 6 times, the relative \mathbf{L}^2 -loss, $\|\mathcal{G}^{\text{ref}} - \mathcal{G}^{\text{approx}}\|_{\mathbf{L}^2} / \|\mathcal{G}^{\text{ref}}\|_{\mathbf{L}^2}$, on the test set is shown in the diagram. A second experiment is presented in Appendix B with similar performance.

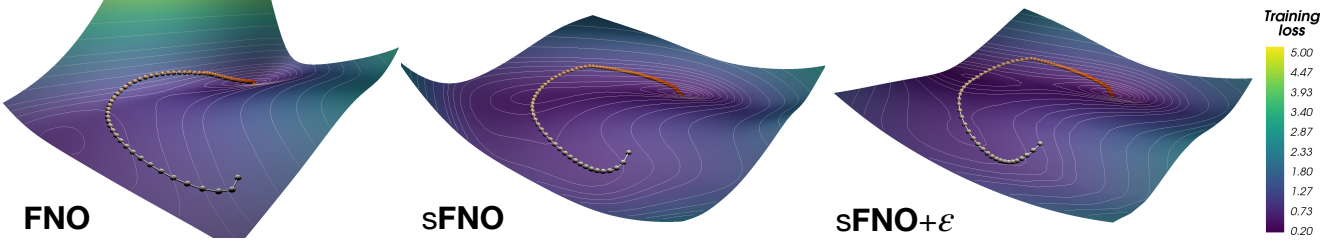


Figure 5: Visual comparison of loss landscapes for 3 of the considered architectures using data in Experiment 1.

As seen in these images, despite their varying degrees of flatness, all the architectures yield qualitatively similar learning trajectories in their respective PCA coordinates. This observation is confirmed when expanding the trajectories’ comparison in a higher-dimensional PCA space, as further discussed in Appendix C.3.

We further refer to Appendix C for more illustrations of wave field reconstructions using each architecture where we also experiment with a different domain configuration and different frequencies for the wave, and multiple random initializations.

All code and data accompanying this manuscript is publicly available at Lara B et al. [2023]

4 Analysis of generalization error bounds

In this section, we analyze the generalization error bounds for Neural Operators and the sequential structure (Section 2.2). For the notation reference, see Appendix A.1.

Let $D \subset \mathbb{R}^d$ be a bounded domain, and $\mathbf{L}^2(D; \mathbb{R}^h)$ be the \mathbf{L}^2 space of \mathbb{R}^h -value function on D . Let $S = \{a_i, u_i\}_{i=1}^n$ be the sequence of independent samples of μ , i.e. $(a_i, u_i) \stackrel{\text{i.i.d}}{\sim} \mu^4$, with marginals μ_a in

⁴Independent Identically Distributed samples drawn from, μ , on $\mathbf{L}^2(D; \mathbb{R}^{d_a}) \times \mathbf{L}^2(D; \mathbb{R}^{d_u})$.

$\mathbf{L}^2(D; \mathbb{R}^{d_a})$ and μ_u in $\mathbf{L}^2(D; \mathbb{R}^{d_u})$. Let \mathcal{G} be the class of Operators mapping from $\mathbf{L}^2(D; \mathbb{R}^{d_a})$ to $\mathbf{L}^2(D; \mathbb{R}^{d_u})$, and $\ell : \mathbf{L}^2(D; \mathbb{R}^{d_u}) \times \mathbf{L}^2(D; \mathbb{R}^{d_a}) \rightarrow \mathbb{R}_{\geq 0}$ be the loss function. Finally, let \mathcal{L} be the Expected risk, and $\hat{\mathcal{L}}_S$ be the Empirical risk defined rigorously in Appendix A.8⁵.

Assumption 4.1. There exists positive constants $\rho > 0$, $R_u > 0$ such that

- (i). ℓ is ρ -Lipschitz continuous, i.e., $|\ell(u_1, v) - \ell(u_2, v)| \leq \rho \|u_1 - u_2\|_{\mathbf{L}^2(D; \mathbb{R}^{d_u})}$ for $u_1, u_2, v \in \mathbf{L}^2(D; \mathbb{R}^{d_u})$.
- (ii). $\ell(\mathbf{0}, \cdot)$ is bounded above by R_u , i.e., $|\ell(\mathbf{0}, u)| \leq R_u$ for $u \in \text{supp}(\mu_u)$ ⁶.

Lemma 4.2. Let Assumption 4.1 holds and suppose there exists $R > 0$ such that

$$\|\mathcal{G}(a)\|_{\mathbf{L}^2(D; \mathbb{R}^{d_u})} \leq R, \quad \forall \mathcal{G} \in \mathcal{G}, \quad a \in \text{supp}(\mu_a), \quad (5)$$

for the hypothesis class, \mathcal{G} . Hence, for any $\delta > \log 2$, the following inequality holds with probability greater than $1 - 2\exp(-\delta)$,

$$\mathcal{L}(\mathcal{G}) \leq \hat{\mathcal{L}}_S(\mathcal{G}) + 2\mathfrak{R}_S(\mathcal{F}_{\mathcal{G}}) + (\rho R + R_u) \sqrt{\frac{2\delta}{n}}, \quad \forall \mathcal{G} \in \mathcal{G}, \quad (6)$$

where $\mathfrak{R}_S(\mathcal{F}_{\mathcal{G}})$ is the (empirical) Rademacher Complexity of the class $\mathcal{F}_{\mathcal{G}}$, see Definition A.10 in Appendix A.8, and the class $\mathcal{F}_{\mathcal{G}}$ is defined by

$$\mathcal{F}_{\mathcal{G}} := \{(a, u) \mapsto \ell(\mathcal{G}(a), u) : (a, u) \in \text{supp}(\mu), \mathcal{G} \in \mathcal{G}\}.$$

Proof. The proof is presented in Appendix D. □

The idea behind the proof is the following, the generalization error $\mathcal{L}(\mathcal{G})$ can be decomposed into $\hat{\mathcal{L}}_S(\mathcal{G})$ and $\mathcal{L}(\mathcal{G}) - \hat{\mathcal{L}}_S(\mathcal{G})$. If the class \mathcal{G} has universal approximation properties, then, $\hat{\mathcal{L}}_S(\mathcal{G})$ can be made "small enough". The term $\mathcal{O}(n^{-1/2})$ decreases as the samples increases. Then, the following is a natural question to ask,

How can we make the Rademacher Complexity, $\mathfrak{R}_S(\mathcal{F}_{\mathcal{G}})$, small?

In the following, we analyze the Rademacher Complexity for standard Neural Operators on functional space, and we compare with our proposed architecture sNO (Section 2.2), whose numerical performance indicates a smaller generalization error for the same number of parameters in Figure 4.

4.1 Related Works of generalization error bounds

There are several references for generalization error bounds for neural networks mapping between finite dimensional spaces, see surveys e.g., Bartlett et al. [2021], Jakubovitz et al. [2019], however, to the best of our knowledge, the generalization error bounds for operators mapping between infinite dimensional spaces have not been fully explored. De Ryck and Mishra [2022] provided the generalization error bound for general operator architectures by employing the Hoeffding's inequality, and they do not involve the analysis of the Rademacher Complexity. On the other hand, Gopalani et al. [2022] and Kim and Kang [2022] have provided that for specific architectures, DeepOnet and FNOs, respectively, by evaluating the Rademacher Complexity.

We remark the previously mentioned works assumed the trainable parameters are finite-dimensional (such as matrices), while our work does not need this assumption. In particular, our infinite-dimensional trainable parameter in the non-local operation is the Lipschitz continuous function in the integral kernel

⁵The Expected risk is defined by the Bochner Integral on $\mathbf{L}^2(D; \mathbb{R}^{d_a}) \times \mathbf{L}^2(D; \mathbb{R}^{d_u})$, see Appendix A.5 and Yoshida [1980].

⁶Support of a measure μ is defined $\text{supp}(\mu) := \{x \in X : \mu(\mathcal{U}) > 0 \text{ for all open neighborhood } \mathcal{U} \text{ of } x\}$ (Cf. Ambrosio et al. [2005, Ch. 5]).

operator. This form is the general Neural Operator, including FNOs, whose Convolutional Integral Operator ansatz yields to an easy implementation. Kim and Kang [2022] assumed the truncated expansion for FNOs, and evaluated the Rademacher Complexity whose upper bounds depend on the number of the truncation. Furthermore, our work not only generalizes Kim and Kang [2022], but also provides to sharper bound of the Rademacher Complexity with the order $\mathcal{O}(1/n^{\frac{1}{d+1}})$ (while order $\mathcal{O}(1)$ in Kim and Kang [2022]).

In order to evaluate the Rademacher Complexity in our setting, we employ the Dudley's Theorem (see e.g., Kakade and Tewari [2008]) and evaluate the covering number for the set of Neural Operators, whose way is different with directly evaluating the Rademacher Complexity like Gopalani et al. [2022], Kim and Kang [2022]. The covering number of Neural Operators is decomposed into that of weights matrices (for the local operation) and Lipschitz continuous function (for the non-local operation). The covering number of matrices and Lipschitz continuous function can be evaluated by using Wainwright [2019] and Gottlieb et al. [2016], respectively.

4.2 Rademacher Complexity of Neural Operators

In this section, we shall analyze the Rademacher Complexity of Neural Operators, [Kovachki et al., 2021b]. Let define the class of standard Neural Operator as follows

$$\mathcal{N} = \left\{ \mathcal{G}_\theta : \mathbf{L}^2(D; \mathbb{R}^{d_a}) \rightarrow \mathbf{L}^2(D; \mathbb{R}^{d_u}) : \mathcal{G}_\theta = (W_L + \mathcal{K}_L) \circ \sigma(W_{L-1} + \mathcal{K}_{L-1}) \circ \cdots \circ \sigma(W_0 + \mathcal{K}_0) \right. \\ \left. W_\ell \in \mathbb{R}^{d_{\ell+1} \times d_\ell}, \text{ and } \mathcal{K}_\ell : \mathbf{L}^2(D; \mathbb{R}^{d_\ell}) \rightarrow \mathbf{L}^2(D; \mathbb{R}^{d_{\ell+1}}), \ell = 0, \dots, L, \text{ and } d_0 = d_a, d_{L+1} = d_u \right\}. \quad (7)$$

$\sigma : \mathbb{R} \rightarrow \mathbb{R}$ is an elementwise nonlinear map, and \mathcal{K}_ℓ are linear integral operators with kernel function, $k_\ell : D \times D \rightarrow \mathbb{R}^{d_{\ell+1} \times d_\ell}$, i.e.,

$$x \mapsto (\mathcal{K}_\ell u)(x) := \int_D k_\ell(x, y) u(y) dy, \quad u \in \mathbf{L}^2(D; \mathbb{R}^{d_\ell}).$$

We shall write, $w_{\ell,ij} = (W_\ell)_{i,j} \in \mathbb{R}$ and $k_{\ell,ij} = (k_\ell)_{i,j} : D \times D \rightarrow \mathbb{R}$ as (i, j) -element of W_ℓ and k_ℓ , respectively.

Assumption 4.3. There exists positive constants $C_w, C_k, C_d, C_a, C_\sigma$, and C_β such that

- (i). $\|W_\ell\|_F \leq C_w$, and $d_\ell \leq C_d$ for all $\ell = 0, \dots, L$, where $\|\cdot\|_F$ is the Frobenius norm.
- (ii). $\|k_\ell\|_{F,\infty} := \sup\{\|k_\ell(x, y)\|_F : x, y \in D\} \leq C_k |D|^{-1}$ for all $\ell = 0, \dots, L$, where $|D| = \int \mathbf{1}_D d\lambda^7$, and $k_\ell : D \times D \rightarrow \mathbb{R}^{n \times m}$ is the kernel function.
- (iii). $\|a\|_{\mathbf{L}^2(D; \mathbb{R}^{d_a})} \leq C_a$ for all $a \in \text{supp}(\mu_a)$.
- (iv). σ is C_σ -Lipschitz, i.e., $|\sigma(s) - \sigma(t)| \leq C_\sigma |s - t|$ for $s, t \in \mathbb{R}$.
- (v). $k_{\ell,ij} : D \times D \rightarrow \mathbb{R}$ is C_β -Lipschitz, see Definition A.4, for $\ell = 0, \dots, L$, $i = 1, \dots, d_\ell^k$, and $j = 1, \dots, d_{\ell+1}^k$.

Under these assumptions, we obtain the following upper bound for Rademacher Complexity for NOs.

Theorem 4.4 (Rademacher Complexity for NOs). *Let suppose assumptions 4.1 and 4.3 hold. Then,*

$$\mathfrak{R}_S(\mathcal{F}_\mathcal{N}) \leq \gamma L^{\frac{\hat{d}+2}{\hat{d}+1}} \{(C_w + C_k)C_\sigma\}^L \left(\frac{1}{n}\right)^{\frac{1}{\hat{d}+1}}, \quad (8)$$

where $\hat{d} := \text{ddim}(D \times D)$ is the doubling number of $D \times D$, and γ is the positive constant independent of L and n , defined in Equation 45.

Proof. The proof is given in Appendix E. □

⁷ λ is the Lebesgue measure.

4.3 Rademacher of sequential Neural Operators

In this section, we analyze the Rademacher Complexity of the sequential structure. We define the sequential structure family, see Section 2.2, as

$$\begin{aligned} \widetilde{\mathcal{N}} = \Big\{ & \mathcal{G}_\theta : \mathbf{L}^2(D; \mathbb{R}^{d_a}) \rightarrow \mathbf{L}^2(D; \mathbb{R}^{d_u}) : \mathcal{G}_\theta = (f_L \circ \mathcal{K}_L) \circ (f_{L-1} \circ \mathcal{K}_{L-1}) \circ \cdots \circ (f_0 \circ \mathcal{K}_0) \\ & f_\ell = W_{\ell,M} \circ \sigma(W_{\ell,M-1}) \circ \cdots \circ \sigma(W_{\ell,0}) \text{ is a Mth layer MLP} \\ & W_{\ell,m} \in \mathbb{R}^{d_{\ell,m+1}^w \times d_{\ell,m}^w} \text{ and } \mathcal{K}_\ell : \mathbf{L}^2(D; \mathbb{R}^{d_\ell^k}) \rightarrow \mathbf{L}^2(D; \mathbb{R}^{d_{\ell+1}^k}) \\ & m = 0, \dots, M, \quad \ell = 0, \dots, L, \quad d_{\ell,0}^w = d_{\ell+1}^k, \quad d_{\ell,M}^w = d_{\ell+1}^k, \quad d_0^k = d_a, \quad d_{L+1}^k = d_u \Big\} \end{aligned} \quad (9)$$

Assumption 4.5. There exists positive constants $C_w, C_k, C_d, C_a, C_\sigma$, and C_β such that

- (i). $\|W_{\ell,m}\|_F \leq C_w$, for $\ell = 0, \dots, L, m = 0, \dots, M$.
- (ii). $\|k_\ell\|_{F,\infty} \leq C_k |D|^{-1}$, for $\ell = 0, \dots, L$.
- (iii). $d_\ell^k, d_{\ell,m}^w \leq C_d$, for $\ell = 0, \dots, L, m = 0, \dots, M$.
- (iv). $\|a\|_{\mathbf{L}^2(D; \mathbb{R}^{d_a})} \leq C_a$, for $a \in \text{supp}(\mu_a)$.
- (v). σ is C_σ -Lipschitz, i.e., $|\sigma(s) - \sigma(t)| \leq C_\sigma |s - t|$ for $s, t \in \mathbb{R}$.
- (vi). $k_{\ell,ij} : D \times D \rightarrow \mathbb{R}$ is C_β -Lipschitz, for $\ell = 0, \dots, L, i = 1, \dots, d_\ell^k$, and $j = 1, \dots, d_{\ell+1}^k$.

Upon these assumptions, we obtain the following upper bound for the Rademacher Complexity of the proposed class, $\widetilde{\mathcal{N}}$.

Theorem 4.6 (Rademacher Complexity of sNO). *Let Assumptions 4.1 and 4.5 hold. Then,*

$$\mathfrak{R}_S(\mathcal{F}_{\widetilde{\mathcal{N}}}) \leq \widetilde{\gamma} L^{\frac{d+2}{d+1}} (C_w^{M+1} C_\sigma^M C_k)^L \left(\frac{1}{n} \right)^{\frac{1}{d+1}}, \quad (10)$$

where $\widetilde{\gamma}$ is the positive constant independent of L and n , defined in 59.

Proof. The proof is given in Appendix F □

4.4 Comparison between standard and sequential Neural Operators

By Lemma 4.2, and Theorems 4.4 and 4.6, we get.

Corollary 4.7. *Let Assumptions 4.1 and 4.3 hold. Then, for any $\delta > \log 2$ and $\mathcal{G} \in \mathcal{N}$, the following inequality holds, with probability greater than $1 - 2 \exp(-\delta)$:*

$$\mathcal{L}(\mathcal{G}) \leq \widehat{\mathcal{L}}_S(\mathcal{G}) + 2\gamma L^{\frac{d+2}{d+1}} \{(C_w + C_k)C_\sigma\}^L \left(\frac{1}{n} \right)^{\frac{1}{d+1}} + (\rho\{(C_w + C_k)C_\sigma\}^L (C_w + C_k)C_a + R_u) \sqrt{\frac{2\delta}{n}}. \quad (11)$$

Proof. The proof is given in Appendix G. □

Corollary 4.8. *Let Assumptions 4.1 and 4.5 hold. Then, for any $\delta > \log 2$ and $\mathcal{G} \in \widetilde{\mathcal{N}}$, the following inequality with probability greater than $1 - 2 \exp(-\delta)$:*

$$\mathcal{L}(\mathcal{G}) \leq \widehat{\mathcal{L}}_S(\mathcal{G}) + 2\widetilde{\gamma} L^{\frac{d+2}{d+1}} (C_w^{M+1} C_\sigma^M C_k)^L \left(\frac{1}{n} \right)^{\frac{1}{d+1}} + (\rho(C_w^{M+1} C_\sigma^M C_k)^L C_w^{M+1} C_\sigma^M C_k C_a + R_u) \sqrt{\frac{2\delta}{n}}. \quad (12)$$

Proof. The proof is given in Appendix G. \square

The first term $\widehat{\mathcal{L}}_S(\mathcal{G})$ can be reduced by training. Both structures have universal approximation properties (see Kovachki et al. [2021b, Theorem 11]). That is, NO can be decomposed into local and non-local, providing an Architecture as sNO, and that the converse is also true (see, Kovachki et al. [2021a, Section 2.5.1]). Albeit, the difference in the generalization error bound has not been studied.

The second and third terms decay as the number n of data goes to infinity with orders $\mathcal{O}(1/n^{\frac{1}{d+1}})$ and $\mathcal{O}(1/n^{\frac{1}{2}})$, respectively. We finally observe the coefficients of n depending on the number L of layers, and conclude the difference between standard and sequential structures as follows:

Corollary 4.9. *Let Assumptions 4.1, 4.3 and 4.5 hold. Also, let suppose $C_w \leq 1$ (corresponding to e.g., dropout), and $C_\sigma \leq 1$ (corresponding to e.g., ReLU activation). Then, $C_w^{M+1}C_\sigma^M C_k \leq (C_w + C_k)C_\sigma$. Furthermore, if L is large (corresponding to deep layers), then $(C_w^{M+1}C_\sigma^M C_k)^L \ll \{(C_w + C_k)C_\sigma\}^L$, which implies that the coefficient of n in (12) is significantly smaller than (11). Therefore, our proposed architecture, would have smaller generalization error.*

Proof. Immediate from Corollaries 4.7 and 4.8. \square

5 Summary and discussion

Scientific computing opens the door to many challenging problems for Machine Learning, and especially for the Deep Learning community, that allows a new world of opportunity to extend already established architectures from finite to infinite dimension (Euclidean to Banach spaces). Neural Operators have recently been proposed as a general framework for Operator Learning with astounding results in some Parametric PDEs problems. However, NOs are the infinite-dimensional counterpart of MLPs, and although MLPs still exist in finite-dimensional Deep Learning, they are seldom used as the main architectures among tasks. Universality is not sufficient to have a flexible, robust, and efficient network (in Euclidean space). Thus, inspired by this observation, we modified the NO towards a so-called *modern* architecture. To this end, we gradually changed NOs towards a Transformer-like NO, which we called (sNO + ε), section 2. We have presented the following results:

- (a) We have shown for computational realizations of NOs in the context of wave propagation that ideas from Transformers significantly reduce the test loss, without losing the approximation property of the network. That is, we showed that FNOs can be substantially improved by small modifications in the arrangement of the layers, and by adding well-known techniques presented in the vast majority of *modern* finite dimensional neural networks.
- (b) We have proved our numerical observations in a theoretical sense, Corollary 4.9. Firstly, by providing an analysis of the generalization error bound of the Neural Operator, Theorem 4.4, and then of the sNO, Theorem 4.6. Our work not only leads to a more general and natural framework to study networks in functional space, but it also provides upper-bound of the Rademacher Complexity of the NO with respect to previous work [Kim and Kang, 2022]; and generalizes other results that considered finite dimensional parameters. Moreover, we have also shown that under assumptions, these (small) changes in sNO yield to a smaller bound in the Rademacher Complexity of the network, without losing the desirable universal property. Providing a solid theoretical setting for the experimental results. Additionally, this might open the door for further modification of NOs or other architectures defined on functional space, as DeepOnet [Lanthaler et al., 2022], with a close statistical theory corroborating the observed results. While showing universality is important, further properties are similarly significant, in order to have networks with greater capacity, and better generalization to unseen data.

- (c) We have considered dataset for time-harmonic wave equation (Section 3.1 and Appendix C.1.3) and have shown that FNO is less efficient than in prototypical elliptic PDEs presented by Li et al. [2020a]. Thus, it is a challenging problem, on which the variation in the architecture has pronounced qualitative (Figures 10 to 12) and quantitative results (Figures 4 and 13).
- (d) Finally, the difference in the performance of $s\text{FNO}+\varepsilon$ and $s\text{FNO}$ lead us to consider the qualitative differences in the loss landscape, building on tools presented by Li et al. [2018a]. Given the high-computational cost of the reconstruction, we only work with the data of our Experiment 1 (cf. Section 3.3). We observed differences in the landscape of the networks, mainly a remarkable flatness in the reconstruction of $s\text{FNO}$ and $s\text{FNO}+\varepsilon$ compared with FNO (Appendix C.3) which is correlated with the generalization of the architectures (Figure 4). However, given the substantial projection, some of the details in the training trajectory are difficult to distinguish, particularly between $s\text{FNO}$ and $s\text{FNO}+\varepsilon$. We intent to explore more efficient ways of visualizing networks in general and in particular networks defined on functional spaces.

Our analysis provides theoretical and numerical evidence that it is possible to construct arrangements in layers for Operator Learning that are more efficient than the direct generalization of feed-forward networks. It implies a more thorough set of considerations when designing networks on functional spaces rather than being limited to the universal approximation property. Although important, it does not take into consideration any Statistics, and thus it is only a partial indicator of the success of the network in applications.

Acknowledgments

J.A.L.B. would like to thank many colleagues at PGS Imaging group for useful discussion during his internship time, and the help on GPU resources. T.F. was supported by Research Grant for Young Scholars funded by yamanashi Prefecture. F.F. acknowledges the use of the cluster PlaFRIM⁸ for the dataset generation. X.M.T. would like to thank the Community Cluster Program and the Rosen Center for Advanced Computing and Purdue. M.V. dH. gratefully acknowledges support from the Department of Energy under grant DE-SC0020345, the Simons Foundation under the MATH + X program, and the corporate members of the Geo-Mathematical Imaging Group at Rice University.

References

- Luigi Ambrosio, Nicola Gigli, and Giuseppe Savaré. *Gradient flows: in metric spaces and in the space of probability measures*. Springer Science & Business Media, 2005.
- George B Arfken and Hans J Weber. *Mathematical methods for physicists*, 1999.
- Emil Artin. *The gamma function*. Courier Dover Publications, 2015.
- Anatolii Borisovich Bakushinsky and M Yu Kokurin. Iterative methods for approximate solution of inverse problems. *Springer Science & Business Media*, 577, 2005.
- Peter L Bartlett, Andrea Montanari, and Alexander Rakhlin. Deep learning: a statistical viewpoint. *Acta numerica*, 30:87–201, 2021.
- Kaushik Bhattacharya, Bamdad Hosseini, Nikola B Kovachki, and Andrew M Stuart. Model reduction and neural networks for parametric pdes. *The SMAI journal of computational mathematics*, 7:121–157, 2021.

⁸<https://www.plafrim.fr/>.

- Vladimir Bogachev. *Gaussian Measures*. Mathematical Surveys and Monographs. American Mathematical Society, 2015.
- Frank Bowman. *Introduction to Bessel functions*. Courier Corporation, 2012.
- Johannes Brandstetter, Rianne van den Berg, Max Welling, and Jayesh K Gupta. Clifford neural layers for pde modeling. *arXiv preprint arXiv:2209.04934*, 2022.
- Shuhao Cao. Choose a transformer: Fourier or galerkin. *Advances in Neural Information Processing Systems*, 34:24924–24940, 2021.
- Masoumeh Dashti and Andrew M Stuart. The bayesian approach to inverse problems. In *Handbook of uncertainty quantification*, pages 311–428. Springer, 2017.
- Tim De Ryck and Siddhartha Mishra. Generic bounds on the approximation error for physics-informed (and) operator learning. *arXiv preprint arXiv:2205.11393*, 2022.
- Jacob Devlin, Ming-Wei Chang, Kenton Lee, and Kristina Toutanova. Bert: Pre-training of deep bidirectional transformers for language understanding. *arXiv preprint arXiv:1810.04805*, 2018.
- Claude R Dietrich and Garry N Newsam. Fast and exact simulation of stationary gaussian processes through circulant embedding of the covariance matrix. *SIAM Journal on Scientific Computing*, 18(4):1088–1107, 1997.
- Alexey Dosovitskiy, Lucas Beyer, Alexander Kolesnikov, Dirk Weissenborn, Xiaohua Zhai, Thomas Unterthiner, Mostafa Dehghani, Matthias Minderer, Georg Heigold, Sylvain Gelly, et al. An image is worth 16x16 words: Transformers for image recognition at scale. *arXiv preprint arXiv:2010.11929*, 2020.
- Björn Engquist and Andrew Majda. Absorbing boundary conditions for numerical simulation of waves. *Proceedings of the National Academy of Sciences*, 74(5):1765–1766, 1977.
- Florian Faucher. hawen: time-harmonic wave modeling and inversion using hybridizable discontinuous galerkin discretization. *Journal of Open Source Software*, 6(57):2699, 2021.
- Florian Faucher and Otmar Scherzer. Adjoint-state method for Hybridizable Discontinuous Galerkin discretization, application to the inverse acoustic wave problem. *Computer Methods in Applied Mechanics and Engineering*, 372:113406, 2020. ISSN 0045-7825. doi: 10.1016/j.cma.2020.113406.
- Florian Faucher, Giovanni Alessandrini, Hélène Barucq, Maarten V de Hoop, Romina Gaburro, and Eva Sincich. Full reciprocity-gap waveform inversion enabling sparse-source acquisition. *Geophysics*, 85(6): R461–R476, 2020.
- Subhashis Ghosal and Aad Van der Vaart. Fundamentals of nonparametric bayesian inference. *Cambridge University Press*, 44, 2017.
- Evarist Giné and Richard Nickl. *Mathematical Foundations of Infinite-Dimensional Statistical Models*, volume 40. Cambridge University Press, 2015.
- Ian Goodfellow, Yoshua Bengio, and Aaron Courville. *Deep learning*. MIT press, 2016.
- Pulkit Gopalani, Sayar Karmakar, and Anirbit Mukherjee. Capacity bounds for the deepnet method of solving differential equations. *arXiv preprint arXiv:2205.11359*, 2022.
- Lee-Ad Gottlieb, Aryeh Kontorovich, and Robert Krauthgamer. Adaptive metric dimensionality reduction. *Theoretical Computer Science*, 620:105–118, 2016.

- Thomas J Grady II, Rishi Khan, Mathias Louboutin, Ziyi Yin, Philipp A Witte, Ranveer Chandra, Russell J Hewett, and Felix J Herrmann. Towards large-scale learned solvers for parametric pdes with model-parallel fourier neural operators. *arXiv preprint arXiv:2204.01205*, 2022.
- Steven Guan, Ko-Tsung Hsu, and Parag V Chitnis. Fourier neural operator networks: A fast and general solver for the photoacoustic wave equation. *arXiv preprint arXiv:2108.09374*, 2021.
- Jan S Hesthaven and Stefano Ubbiali. Non-intrusive reduced order modeling of nonlinear problems using neural networks. *Journal of Computational Physics*, 363:55–78, 2018.
- Gao Huang, Yu Sun, Zhuang Liu, Daniel Sedra, and Kilian Q Weinberger. Deep networks with stochastic depth. In *European conference on computer vision*, pages 646–661. Springer, 2016.
- Daniel Jakubovitz, Raja Giryes, and Miguel RD Rodrigues. Generalization error in deep learning. In *Compressed sensing and its applications*, pages 153–193. Springer, 2019.
- Sham Kakade and Ambuj Tewari. Dudley’s theorem, fat shattering dimension, packing numbers. *Lecture 15, Toyota Technological Institute at Chicago*, 2008.
- Barbara Kaltenbacher, Andreas Neubauer, and Otmar Scherzer. Iterative regularization methods for nonlinear ill-posed problems. In *Iterative Regularization Methods for Nonlinear Ill-Posed Problems*. de Gruyter, 2008.
- George Em Karniadakis, Ioannis G Kevrekidis, Lu Lu, Paris Perdikaris, Sifan Wang, and Liu Yang. Physics-informed machine learning. *Nature Reviews Physics*, 3(6):422–440, 2021.
- Salman Khan, Muzammal Naseer, Munawar Hayat, Syed Waqas Zamir, Fahad Shahbaz Khan, and Mubarak Shah. Transformers in vision: A survey. *ACM Computing Surveys (CSUR)*, 2021.
- Taeyoung Kim and Myungjoo Kang. Bounding the rademacher complexity of fourier neural operator. *arXiv preprint arXiv:2209.05150*, 2022.
- Diederik P Kingma and Jimmy Ba. Adam: A method for stochastic optimization. *arXiv preprint arXiv:1412.6980*, 2014.
- Georgios Kissas, Jacob H Seidman, Leonardo Ferreira Guilhoto, Victor M Preciado, George J Pappas, and Paris Perdikaris. Learning operators with coupled attention. *Journal of Machine Learning Research*, 23 (215):1–63, 2022.
- Nikola Kovachki, Samuel Lanthaler, and Siddhartha Mishra. On universal approximation and error bounds for fourier neural operators. *Journal of Machine Learning Research*, 22:Art–No, 2021a.
- Nikola Kovachki, Zongyi Li, Burigede Liu, Kamyar Azizzadenesheli, Kaushik Bhattacharya, Andrew Stuart, and Anima Anandkumar. Neural operator: Learning maps between function spaces. *arXiv preprint arXiv:2108.08481*, 2021b.
- Prashant Kumar. Gaussian random fields with matern covariance parametrization. <https://github.com/pks19/Gaussian-random-fields>, 2019.
- Thorsten Kurth, Shashank Subramanian, Peter Harrington, Jaideep Pathak, Morteza Mardani, David Hall, Andrea Miele, Karthik Kashinath, and Animashree Anandkumar. Fourcastnet: Accelerating global high-resolution weather forecasting using adaptive fourier neural operators. *arXiv preprint arXiv:2208.05419*, 2022.

- Samuel Lanthaler, Siddhartha Mishra, and George E Karniadakis. Error estimates for deepnets: A deep learning framework in infinite dimensions. *Transactions of Mathematics and Its Applications*, 6(1):tnac001, 2022.
- J Antonio Lara B, Florian Faucher, and Xavier Tricoche. Official repo: Fine tuning neural operators. <https://github.com/JALB-epsilon/Fine-tuning-N0s>, 2023.
- James Lee-Thorp, Joshua Ainslie, Ilya Eckstein, and Santiago Ontanon. Fnet: Mixing tokens with fourier transforms. *arXiv preprint arXiv:2105.03824*, 2021.
- Bian Li, Hanchen Wang, Xiu Yang, and Youzuo Lin. Solving seismic wave equations on variable velocity models with fourier neural operator. *arXiv preprint arXiv:2209.12340*, 2022a.
- Hao Li, Zheng Xu, Gavin Taylor, Christoph Studer, and Tom Goldstein. Visualizing the loss landscape of neural nets. *Advances in neural information processing systems*, 31, 2018a.
- Hao Li, Zheng Xu, Gavin Taylor, Christoph Studer, and Tom Goldstein. Visualizing the loss landscape of neural nets. <https://github.com/tomgoldstein/loss-landscape>, 2018b.
- Zhijie Li, Wenhui Peng, Zelong Yuan, and Jianchun Wang. Fourier neural operator approach to large eddy simulation of three-dimensional turbulence. *Theoretical and Applied Mechanics Letters*, 12(6):100389, 2022b.
- Zongyi Li, Nikola Kovachki, Kamyar Azizzadenesheli, Burigede Liu, Kaushik Bhattacharya, Andrew Stuart, and Anima Anandkumar. Fourier neural operator for parametric partial differential equations. *arXiv preprint arXiv:2010.08895*, 2020a.
- Zongyi Li, Nikola Kovachki, Kamyar Azizzadenesheli, Burigede Liu, Kaushik Bhattacharya, Andrew Stuart, and Anima Anandkumar. Neural operator: Graph kernel network for partial differential equations. *arXiv preprint arXiv:2003.03485*, 2020b.
- Ze Liu, Yutong Lin, Yue Cao, Han Hu, Yixuan Wei, Zheng Zhang, Stephen Lin, and Baining Guo. Swin transformer: Hierarchical vision transformer using shifted windows. *Proceedings of the IEEE/CVF International Conference on Computer Vision*, pages 10012–10022, 2021.
- Zhuang Liu, Hanzi Mao, Chao-Yuan Wu, Christoph Feichtenhofer, Trevor Darrell, and Saining Xie. A convnet for the 2020s. *Proceedings of the IEEE/CVF Conference on Computer Vision and Pattern Recognition*, pages 11976–11986, 2022.
- Gabriel J Lord, Catherine E Powell, and Tony Shardlow. *An introduction to computational stochastic PDEs*, volume 50. Cambridge University Press, 2014.
- Lu Lu, Pengzhan Jin, Guofei Pang, Zhongqiang Zhang, and George Em Karniadakis. Learning nonlinear operators via deepnet based on the universal approximation theorem of operators. *Nature Machine Intelligence*, 3(3):218–229, 2021.
- Lu Lu, Xuhui Meng, Shengze Cai, Zhiping Mao, Somdatta Goswami, Zhongqiang Zhang, and George Em Karniadakis. A comprehensive and fair comparison of two neural operators (with practical extensions) based on fair data. *Computer Methods in Applied Mechanics and Engineering*, 393:114778, 2022.
- Paul A Martin. *Time-Domain Scattering*, volume 180. Cambridge University Press, 2021.
- Gen Nakamura and Roland Potthast. Inverse modeling. *IOP Publishing*, 2015.

- Richard Nickl and Sven Wang. On polynomial-time computation of high-dimensional posterior measures by langevin-type algorithms. *arXiv preprint arXiv:2009.05298*, 2020.
- Jaideep Pathak, Shashank Subramanian, Peter Harrington, Sanjeev Raja, Ashesh Chattopadhyay, Morteza Mardani, Thorsten Kurth, David Hall, Zongyi Li, Kamyar Azizzadenesheli, et al. Fourcastnet: A global data-driven high-resolution weather model using adaptive fourier neural operators. *arXiv preprint arXiv:2202.11214*, 2022.
- Maziar Raissi, Paris Perdikaris, and George E Karniadakis. Physics-informed neural networks: A deep learning framework for solving forward and inverse problems involving nonlinear partial differential equations. *Journal of Computational physics*, 378:686–707, 2019.
- Mark Sandler, Andrew Howard, Menglong Zhu, Andrey Zhmoginov, and Liang-Chieh Chen. Mobilenetv2: Inverted residuals and linear bottlenecks. In *Proceedings of the IEEE conference on computer vision and pattern recognition*, pages 4510–4520, 2018.
- Nitish Srivastava, Geoffrey Hinton, Alex Krizhevsky, Ilya Sutskever, and Ruslan Salakhutdinov. Dropout: a simple way to prevent neural networks from overfitting. *The journal of machine learning research*, 15(1):1929–1958, 2014.
- Andrew M Stuart. Inverse problems: a bayesian perspective. *Acta numerica*, 19:451–559, 2010.
- Tapas Tripura and Souvik Chakraborty. Wavelet neural operator: a neural operator for parametric partial differential equations. *arXiv preprint arXiv:2205.02191*, 2022.
- Ashish Vaswani, Noam Shazeer, Niki Parmar, Jakob Uszkoreit, Llion Jones, Aidan N Gomez, Łukasz Kaiser, and Illia Polosukhin. Attention is all you need. *Advances in neural information processing systems*, 30, 2017.
- Martin J. Wainwright. *High-Dimensional Statistics: A Non-Asymptotic Viewpoint*. Cambridge Series in Statistical and Probabilistic Mathematics. Cambridge University Press, 2019.
- Gege Wen, Zongyi Li, Kamyar Azizzadenesheli, Anima Anandkumar, and Sally M Benson. U-fno—an enhanced fourier neural operator-based deep-learning model for multiphase flow. *Advances in Water Resources*, 163:104180, 2022a.
- Gege Wen, Zongyi Li, Qirui Long, Kamyar Azizzadenesheli, Anima Anandkumar, and Sally M Benson. Accelerating carbon capture and storage modeling using fourier neural operators. *arXiv preprint arXiv:2210.17051*, 2022b.
- Yan Yang, Angela F Gao, Jorge C Castellanos, Zachary E Ross, Kamyar Azizzadenesheli, and Robert W Clayton. Seismic wave propagation and inversion with neural operators. *The Seismic Record*, 1(3): 126–134, 2021.
- Ziyi Yin, Ali Siahkoohi, Mathias Louboutin, and Felix J Herrmann. Learned coupled inversion for carbon sequestration monitoring and forecasting with fourier neural operators. *arXiv preprint arXiv:2203.14396*, 2022.
- Kôsaku Yoshida. *Functional Analysis*. Classics in mathematics. Springer, 1980.
- Huaiqian You, Quinn Zhang, Colton J Ross, Chung-Hao Lee, and Yue Yu. Learning deep implicit fourier neural operators (ifnos) with applications to heterogeneous material modeling. *arXiv preprint arXiv:2203.08205*, 2022.

Weihao Yu, Mi Luo, Pan Zhou, Chenyang Si, Yichen Zhou, Xinchao Wang, Jiashi Feng, and Shuicheng Yan. Metaformer is actually what you need for vision. In *Proceedings of the IEEE/CVF Conference on Computer Vision and Pattern Recognition*, pages 10819–10829, 2022.

Appendix

A Preliminaries

A.1 Notation

Notation	Meaning
d	Dimension of spatial domain
d_a	Dimension of input function $a(x)$
d_u	Dimension of output function $u(x)$
d_ℓ	Number of the column for W_ℓ
$d_{\ell,m}^w$	Number of the column for $W_{\ell,m}$
d_ℓ^k	Number of the column for $k_\ell(x, y)$
$D \subset \mathbb{R}^d$	Spatial domain
$a \in \mathbf{L}^2(D; \mathbb{R}^{d_a})$	Input function
$u \in \mathbf{L}^2(D; \mathbb{R}^{d_u})$	Output function
n	Number of training data
$S = \{a_i, u_i\}_{i=1}^n$	Training dataset drawn from probability measure μ
μ	Probability measure on $\mathbf{L}^2(D; \mathbb{R}^{d_a}) \times \mathbf{L}^2(D; \mathbb{R}^{d_u})$
μ_a	Marginals of μ on $\mathbf{L}^2(D; \mathbb{R}^{d_a})$
μ_u	Marginals of μ on $\mathbf{L}^2(D; \mathbb{R}^{d_u})$
ℓ	Loss function
σ	Activation function
\mathcal{N}	Space of Neural Operators
W_ℓ	$d_{\ell+1} \times d_\ell$ -matrix in \mathcal{N}
\mathcal{K}_ℓ	Integral operator with kernel k_ℓ in \mathcal{N}
k_ℓ	$d_{\ell+1} \times d_\ell$ -kernel matrix for \mathcal{K}_ℓ
L	Number of layers
\hat{d}	Doubling number of $D \times D$
$\widetilde{\mathcal{N}}$	Space of sequential Neural Operators
f_ℓ	MLPs in $\widetilde{\mathcal{N}}$
M	Number of layers in MLPs f_ℓ
$W_{\ell,m}$	$d_{\ell,m+1}^w \times d_{\ell,m}^w$ -matrix in MLPs f_ℓ
k_ℓ	$d_{\ell+1}^k \times d_\ell^k$ -kernel matrix in $\widetilde{\mathcal{N}}$
$\mathbf{L}^2(D; \mathbb{R}^h)$	L^2 space of \mathbb{R}^h -value function on D
$\ \cdot\ _{\mathbf{L}^2(D; \mathbb{R}^h)}$	L^2 -norm
$\ \cdot\ _2$	ℓ_2 -norm
$\ \cdot\ _F$	Frobenius norm
$\ \cdot\ _S$	Sampling norm, $\ f\ _S := \left(\frac{1}{n} \sum_{i=1}^n f(a_i, u_i)^2\right)^{\frac{1}{2}}$
$\ \cdot\ _{\text{op}}$	Operator norm

Table 1: Table of Notations

A.2 Vector-Valued L^2 spaces

$\mathbf{L}^2(D; \mathbb{R}^{d_a})$ is the \mathbf{L}^2 space of \mathbb{R}^{d_a} -value function on $D \subset \mathbb{R}^d$. It is defined as the space of functions such that,

$$\|a\|_{\mathbf{L}^2(D; \mathbb{R}^{d_a})}^2 := \int_D \|a(x)\|_2^2 dx < \infty,$$

where $D \ni x \mapsto \|a(x)\|_2^2 = \sum_j a_j^2(x)$; notices that, $\|\cdot\|_2^2$ is the usual ℓ_2 -norm in \mathbb{R}^{d_a} .

A.3 Linear Bounded Operator

Definition A.1 (Linear Bounded Operator). We say that $\mathbf{A} : X \rightarrow Y$ is the Linear Bounded Operator mapping from a Banach spaces X to a Banach space Y , if it is linear and if there exists a positive constant $C > 0$ such that,

$$\|\mathbf{A}x\|_Y \leq C\|x\|_X, \quad x \in X.$$

Definition A.2 (Operator norm). We also recall that the Operator norm $\|\mathbf{A}\|_{\text{op}}$ for linear bounded operator \mathbf{A} as

$$\|\mathbf{A}\|_{\text{op}} := \inf \{C \in \mathbb{R}_{\geq 0} \mid \|\mathbf{A}x\|_Y \leq C\|x\|_X\}.$$

In particular, Neural Operators [Li et al., 2020a] include the Linear Integral Bounded Operator

Definition A.3 (Linear Integral Bounded Operator). It is an Linear Bounded Operator $\mathcal{K} : \mathbf{L}^2(D; \mathbb{R}^n) \rightarrow \mathbf{L}^2(D; \mathbb{R}^m)$ defined by

$$x \mapsto (\mathcal{K}g)(x) := \int_D k(x, y) g(y) dy, \quad x \in D, \quad g \in \mathbf{L}^2(D; \mathbb{R}^n),$$

where $k : D \times D \subset \mathbb{R}^{d \times d} \rightarrow \mathbb{R}^{m \times n}$ is the Integral Kernel.

Definition A.4 (Lipschitz Kernel). We say a vector-valued Integral Kernel is Lipschitz continuous, if there exists $C > 0$ such that

$$|k_{i,j}(x, y) - k_{i,j}(x', y')| \leq C \|(x, y) - (x', y')\|_2, \quad (x, y), (x', y') \in D \times D.$$

for $i, j \in \{1, \dots, d\}$.

A.4 Neural Operator

Let D a bounded domain and let $\mathcal{A}(D; \mathbb{R}^{d_a})$, $\mathcal{U}(D; \mathbb{R}^{d_{v_i}})$, and $\mathcal{U}(D; \mathbb{R}^{d_u})$ be abstract (separable) Banach spaces.

Definition A.5 (Neural Operator). Let define $\mathcal{G}_\theta : \mathcal{A}(D; \mathbb{R}^{d_a}) \rightarrow \mathcal{U}(D; \mathbb{R}^{d_u})$ such that

$$u = \mathcal{G}_\theta(a) = \mathcal{Q} \circ \mathcal{L}_k \circ \dots \circ \mathcal{L}_1 \circ \mathcal{R}(a), \quad (13)$$

in where $\mathcal{R} : \mathcal{A}(D; \mathbb{R}^{d_a}) \rightarrow \mathcal{U}(D; \mathbb{R}^{d_{v_1}})$ (Lifting map), and $\mathcal{Q} : \mathcal{U}(D; \mathbb{R}^{d_{v_{k+1}}}) \rightarrow \mathcal{U}(D; \mathbb{R}^{d_u})$ (Projection map), such that

$$\mathcal{R}(a)(x) := (Ra(x)), \quad R \in \mathbb{R}^{d_{v_1} \times d_a}. \quad (14a)$$

$$\mathcal{Q}(v)(x) := (Qv(x)), \quad Q \in \mathbb{R}^{d_u \times d_{v_{k+1}}}. \quad (14b)$$

and \mathcal{L}_i , ($i = 1, \dots, k$) is defined as

$$D \ni x \mapsto (\mathcal{L}_i v)(x) := (W_i v(x) + (\mathcal{K}_i v)(x)), \quad W_i \in \mathbb{R}^{v_{i+1} \times v_i}. \quad (\text{Layers})$$

$i = 1, \dots, k$, and \mathcal{K}_i is an integral operator mapping from $\mathcal{U}(D; \mathbb{R}^{d_{v_i}})$ to $\mathcal{U}(D; \mathbb{R}^{d_{v_{i+1}}})$, see definition A.3. In the definition of Kovachki et al. [2021b, Section 9.1], Neural Operators parameterize the integral kernel as neural networks which satisfies the Lipschitz continuity used in the Assumption 4.5.

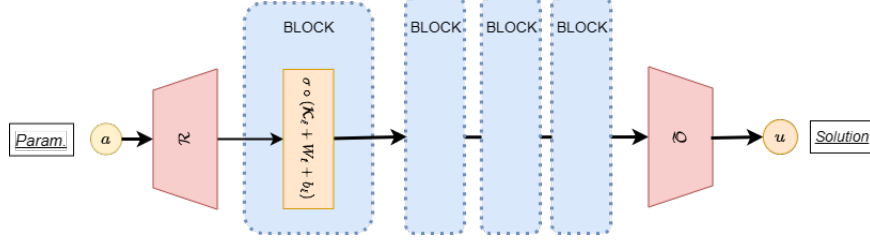


Figure 6: NO. Neural Operator architecture.

A.4.1 Fourier Neural Operators (FNOs)

A natural ansatz in the integral operator is assuming to be convolutional, so that,

$$(k * v) = \mathcal{F}^{-1}(\mathcal{F}(k) \cdot \mathcal{F}(v)). \quad (15)$$

⁹ if the kernel function and v lies on the adequate space, say \mathbf{L}^2 . When Equation 15 is estimated by the FFT algorithm, the Neural Operator is efficiently implemented, leading to the network presented in Li et al. [2020a].

A.5 Bochner integral

In the study of generalization error bounds, the Expected error, see Appendix A.8, is defined through the Bochner Integral. We briefly introduce it, informally, is the natural generalization of the Lebesgue integral on (separables) Banach spaces.

For our purpose, it suffices to define the integral (informally) on $\mathbf{L}^2(D; \mathbb{R}^{d_a}) \times \mathbf{L}^2(D; \mathbb{R}^{d_u})$. Assume that a function $(a, u) \mapsto f(a, u) \in \mathbb{R}$ is Bochner integrable with respect to the measure μ on $\mathbf{L}^2(D; \mathbb{R}^{d_a}) \times \mathbf{L}^2(D; \mathbb{R}^{d_u})$, i.e., there exists a sequence of Integrable simple functions s_n (the finite linear combination of indicator functions of measurable sets) such that

$$\lim_{n \rightarrow \infty} \int |f(a, u) - s_n(a, u)| d\mu(a, u) = 0.$$

Thus, the Bochner Integral is defined by

$$\int \ell(\mathcal{G}(a), u) d\mu(a, u) = \lim_{n \rightarrow \infty} \int s_n(a, u) d\mu(a, u).$$

For a detailed (formal) definition of the Bochner integral, as well as its properties, see Yoshida [1980].

A.6 Gaussian Measure

The typical choice of the measure μ in the context of PDEs is the Gaussian Measure, which will be reviewed as follows (refer to e.g., Stuart [2010, Section 6]): First, a function $m \in X$ is called the mean of μ if for all $\ell \in X^*$, where X^* denote the dual space of linear functionals on X ,

$$\ell(m) = \int_X \ell(x) d\mu(x),$$

where the integral in the right hand side is defined by Bocher integral (see Appendix A.5) on X with respect to μ . A linear operator $\mathcal{C} : X^* \rightarrow X$ is called the Covariance Operator if for all $k, \ell \in X^*$,

$$k(\mathcal{C}\ell) = \int_X k(x - m)\ell(x - m) d\mu(x).$$

⁹ \mathcal{F} , and \mathcal{F}^{-1} represents the Fourier and Inverse Fourier transform respectively.

We say that u draws from *Gaussian Measure* $\mathcal{N}(m, \mathcal{C})$ (write $u \sim \mathcal{N}(m, \mathcal{C})$) if for all $\ell \in X^*$, $\ell(u)$ draws from the one-dimensional Gaussian distribution $\mathcal{N}(\ell(m), \ell(\mathcal{C}\ell))$.

If X is a Hilbert space, then we can characterize random draws from a Gaussian Measure by using the *Karhunen-Loève expansion* as follows (see e.g., Stuart [2010, Theorem 6.19]):

Theorem A.6. *Let X be a Hilbert space, and let $\mathcal{C} : X \rightarrow X$ be a self-adjoint, positive semi-definite, compact operator, and let $m \in X$. Let $\{\phi_k, \gamma_k\}_{k=1}^\infty$ be an orthonormal set of eigenvectors and eigenvalues for \mathcal{C} ordered so that*

$$\gamma_1 \geq \gamma_2 \geq \dots.$$

Take $\{\xi_k\}_{k=1}^\infty$ to be an i.i.d. sequence with $\xi_1 \sim \mathcal{N}(0, 1)$. Then, the random variable $u \in X$ given by the Karhunen-Loève expansion

$$u = m + \sum_{k=1}^{\infty} \sqrt{\gamma_k} \xi_k \phi_k \quad (16)$$

draws from $\mathcal{N}(m, \mathcal{C})$.

A.7 Gaussian Random Field

Let $(\Omega, \mathcal{F}, \mathbb{P})$ be a probability space. We say that a function $u : D \times \Omega \rightarrow \mathbb{R}$ is a Gaussian Random Field (GRF) if $u(x, \cdot) \in L^2(\Omega)$, and for any $x_1, \dots, x_M \in D$ and any $M \in \mathbb{N}$,

$$\mathbf{u}_M := (u(x_1, \cdot), \dots, u(x_M, \cdot))^T$$

draws from the multivariate Gaussian distribution $\mathcal{N}(\mathbf{m}_M, \mathcal{C}_M)$. Here, $m(x) := \mathbb{E}_\omega[u(x, \omega)]$ is the mean function, and $c(x, y) = \mathbb{E}_\omega[(u(x, \omega) - m(x))(u(y, \omega) - m(y))^*]$ is the covariance function. We have denoted by $\mathbf{m}_M := (m_1, \dots, m_M)^T$ and $\mathcal{C}_M = (c_{ij})_{i,j=1}^M$, where $m_i := m(x_i)$, and $c_{ij} := c(x_i, x_j)$. The GRF also has the Karhunen-Loève expansion with (16) as $X = L^2(D)$, m is the mean function, and \mathcal{C} is the integral operator with the kernel given by the covariance function (see Lord et al. [2014, Theorem 7.52]).

We can construct the GRF drawing from a certain Gaussian Measure. We simply consider the Gaussian Measure $\mathcal{N}(0, (-\Delta)^{-\alpha})$ where Δ is the Laplacian with domain $H_0^1(D) \cap H^2(D)$ where $D = [0, 1]^2$ and $\alpha > 1$. Then, the draw u from $\mathcal{N}(0, (-\Delta)^{-\alpha})$ are almost surely in $C(D)$ (see Stuart [2010, Example 6.28]), which means that the function u can be point-wisely defined, and then, for any $x_1, \dots, x_M \in D$ and any $M \in \mathbb{N}$, $(u(x_1, \cdot), \dots, u(x_M, \cdot))^T$ draws from the multivariate Gaussian distribution, that is, u is the GRF.

A.8 Expected/ Empirical Loss

Definition A.7 (Expected Risk/Loss). The Expected risk is defined by the Bochner Integral, see Appendix A.5.

$$\mathcal{L}(\mathcal{G}) := \mathbb{E}_{(a,u) \sim \mu} [\ell(\mathcal{G}(a), u)] = \int \ell(\mathcal{G}(a), u) d\mu(a, u),$$

with respect to $\mathcal{G} \in \mathcal{G}$, where the set \mathcal{G} is the Hypothesis class. For this purpose of this paper, the class corresponds to Neural Operators or sequential Neural Operators, and $\ell : \mathbf{L}^2(D; \mathbb{R}^{d_u}) \times \mathbf{L}^2(D; \mathbb{R}^{d_a}) \rightarrow [0, \infty)$ is the loss function.

Definition A.8 (Empirical Risk/Loss). It is defined as the unbiased estimator of the Expected risk, that is

$$\hat{\mathcal{L}}_S(\mathcal{G}) := \frac{1}{n} \sum_{i=1}^n \ell(\mathcal{G}(a_i), u_i),$$

where $(a_i, u_i) \stackrel{\text{i.i.d.}}{\sim} \mu$.

The generalization error $\mathcal{L}(\mathcal{G})$ is decomposed into $\widehat{\mathcal{L}}_S(\mathcal{G})$ and $\mathcal{L}(\mathcal{G}) - \widehat{\mathcal{L}}_S(\mathcal{G})$. The difference, $\mathcal{L}(\mathcal{G}) - \widehat{\mathcal{L}}_S(\mathcal{G})$ between the generalization and empirical errors is evaluated using the Uniform Laws of Large Numbers (see e.g., Theorem 4.10 in [Wainwright, 2019] or Theorem 3.4.5 in [Giné and Nickl, 2015]).

Lemma A.9 (Uniform Laws of Large Numbers). *Let \mathcal{F} be the set of measurable functions on a measurable space (S, \mathcal{S}) with absolute values bounded by R , let X_i ($i \in \mathbb{N}$) be i.i.d. S -valued random variables with common probability law \mathbf{P} , and let ϵ_i ($i \in \mathbb{N}$) be a sequence of i.i.d Rademacher RVs, i.e., ϵ_i are independent, and $\mathbf{P}\{\epsilon_i = 1\} = 1/2 = \mathbf{P}\{\epsilon_i = -1\}$. Then, for all $n \in \mathbb{N}$ and $\delta > 0$, the following inequality holds with probability greater than $1 - 2\exp(-\delta)$,*

$$\sup_{f \in \mathcal{F}} \left| \frac{1}{n} \sum_{i=1}^n f(X_i) - \mathbb{E}[f(X)] \right| \leq 2\mathfrak{R}_S(\mathcal{F}) + R\sqrt{\frac{2\delta}{n}},$$

where $\mathfrak{R}_S(\mathcal{F})$ is the Rademacher Complexity of the class \mathcal{F} defined above.

The Rademacher Complexity $\mathfrak{R}_S(\mathcal{F})$ of the class \mathcal{F} is defined as follows.

Definition A.10. (Rademacher Complexity) Let \mathcal{F} be the set of measurable functions on a measurable space (S, \mathcal{S}) . Let $\{\epsilon_i\}_{i=1}^n$ is a sequence of i.i.d. RV's with Rademacher distribution; i.e., $\mathbf{P}\{\epsilon_i = 1\} = 1/2 = \mathbf{P}\{\epsilon_i = -1\}$. The Rademacher Complexity of the class \mathcal{F} is defined as

$$\mathfrak{R}_S(\mathcal{F}) := \mathbb{E}_{\epsilon \sim \text{Rad}} \left[\sup_{f \in \mathcal{F}} \frac{1}{n} \left| \sum_{i=1}^n \epsilon_i f(a_i, u_i) \right| \right],$$

(Cf. Giné and Nickl [2015, Definition 3.1.19]).

Intuitively, Rademacher complexity $\mathfrak{R}_S(\mathcal{F})$ measures richness of a class \mathcal{F} of real-valued functions.

Definition A.11 (Covering Number). Let $(\mathcal{F}, \|\cdot\|)$ be a normed vector space. We define, $N(\varepsilon, \mathcal{F}, \|\cdot\|)$, the covering number of \mathcal{F} (sometimes known as entropy number) which means the minimal cardinality of a subset $\mathcal{C} \subset \mathcal{F}$ that covers \mathcal{F} at scale ε with respect to the norm $\|\cdot\|$.

Roughly speaking, the covering number $N(\varepsilon, \mathcal{F}, \|\cdot\|)$ is the necessary number of ε -balls with respect to norm $\|\cdot\|$ to completely cover a space \mathcal{F} (see e.g., Wainwright [2019, Definition 5.1]). Furthermore, it is possible to estimate Rademacher Complexity $\mathfrak{R}_S(\mathcal{F})$ by using the *covering number*. The following lemma is known as *Dudley's Theorem*.

Lemma A.12 (Dudley's Theorem). *Let \mathcal{F} be the set of real-valued function. Then,*

$$\mathfrak{R}_S(\mathcal{F}) \leq \inf_{\alpha \geq 0} \left\{ 4\alpha + \frac{12}{\sqrt{n}} \int_{\alpha}^{\infty} \sqrt{\log N(\varepsilon, \mathcal{F}, \|\cdot\|_S)} d\varepsilon \right\}$$

where $\|f\|_S := \left(\frac{1}{n} \sum_{i=1}^n f(X_i)^2 \right)^{1/2}$.

The main results in this paper is to apply these lemmas as \mathcal{F} is the set of loss function $\ell(\mathcal{G}(\cdot), \cdot)$ where \mathcal{G} is the class of Neural Operators or sequential Neural Operators. Neural Operators \mathcal{G} is parameterized by weight matrices and Lipschitz continuous functions, and finally we will arrive at evaluating of the covering number of them, which are referred to [Wainwright, 2019].

A.9 Interpretation of the skip Connection for Operators defined through PDEs

For the data generated on this paper, we consider (non-linear) Operators between (separable) Banach Spaces defined implicitly through PDEs of the following form

$$\mathbf{L}_a u(x) = f(x), \quad x \text{ in } D, \quad (17a)$$

$$\mathbf{B}u(x) = 0, \quad x \text{ on } \partial D, \quad (17b)$$

where $D \subset \mathbb{R}^d$ is a bounded domain, \mathbf{L}_a is a Partial Differential Operator whose coefficient $a \in \mathcal{A}(D; \mathbb{R}^{d_a}) := \{a : D \subset \mathbb{R}^d \rightarrow \mathbb{R}^{d_a}\}$. \mathbf{B} is some Boundary Operator (Dirichlet, Neumann, among others). $u \in \mathcal{U}(D; \mathbb{R}^{d_u}) := \{u : D \subset \mathbb{R}^d \rightarrow \mathbb{R}^{d_u}\}$ is a solution field, and $f \in \mathcal{U}(D; \mathbb{R}^{d_u})^*$ is a fixed function. $\mathcal{U}(D; \mathbb{R}^{d_u})^*$ is the dual space of $\mathcal{U}(D; \mathbb{R}^{d_u})$.

We often translate the forward problem into solving the following implicit equations (by using e.g., variational formulations and integral equations):

$$\mathcal{J}(u) = 0, \quad (18)$$

where $\mathcal{J} : \mathcal{U}(D; \mathbb{R}^{d_u}) \rightarrow \mathbb{R}$ is a nonlinear mapping. The solution of (18) is given by Newton's method [Bakushinsky and Kokurin, 2005, Kaltenbacher et al., 2008, Nakamura and Potthast, 2015], that is,

$$u_{k+1} = u_k - (\mathcal{J}'(u_k))^{-1} \mathcal{J}(u_k) =: u_k + \mathfrak{D}(u_k), \quad k = 0, 1, \dots \quad (19)$$

Here, u_0 are some initial guesses and $(\mathcal{J}'(u_k))^{-1}$ is the inverse of a linear operator $\mathcal{J}'(u_k)$, where $\mathcal{J}'(u_k) : \mathcal{U}(D; \mathbb{R}^{d_u}) \rightarrow \mathbb{R}$ is the Fréchet derivative of \mathcal{J} at u_k .

Our proposed architecture includes the skip-connection in order not only to make training stable, but also to mimic the Newton iterations: u_{k+1} and u_k correspond to the output and input, respectively, in one layer, and u_{k+1} is constructed by adding u_k (corresponding the skip-connection) to $\mathfrak{D}(u_k)$ (corresponding to the composition of layer normalization and non-local or local operations, see Figure 2), and getting the architecture deeper corresponds to iteration steps k repeated many times.

B Time-harmonic acoustic wave dataset

Our dataset corresponds to the propagation of waves associated with an acoustic medium characterized by a wave speed. The waves, more precisely pressure field, are given at specific frequencies and known source.

B.1 Time-harmonic wave equations

We consider the propagation of time-harmonic acoustic waves for two dimensional domain $D \subset \mathbb{R}^2$. The waves are given by the (scalar) pressure field p and (vector) particle velocity \mathbf{v} solutions to [Faucher and Scherzer, 2020, Martin, 2021]

$$\begin{cases} -i\omega\rho(\mathbf{x})\mathbf{v}(\mathbf{x},\omega) - \nabla p(\mathbf{x},\omega) = 0, & \text{in } D, \\ -\frac{i\omega}{\kappa(\mathbf{x})}p(\mathbf{x},\omega) + \nabla \cdot \mathbf{v}(\mathbf{x},\omega) = f(\mathbf{x},\omega), & \text{in } D, \end{cases} \quad (20a)$$

where f is the time-harmonic source of angular frequency ω , ρ is the density and κ the bulk modulus. The angular frequency is ω . The boundary of the domain $\partial D = \Gamma_1 \cup \Gamma_2$ is separated into two, following a geophysical configuration: a free-surface condition is imposed at the surface Γ_1 (that is the interface between

the medium and the air), while absorbing boundary conditions [Engquist and Majda, 1977] are imposed elsewhere (that is, to truncate the numerical domain), see Figure 7. These correspond to conditions

$$p(\mathbf{x}, \omega) = 0, \quad \text{on } \Gamma_1 \text{ (free surface),} \quad (21a)$$

$$\partial_\nu p(\mathbf{x}, \omega) - \frac{i\omega}{c(\mathbf{x})} p(\mathbf{x}, \omega) = 0, \quad \text{on } \Gamma_2 \text{ (absorbing boundary conditions).} \quad (21b)$$

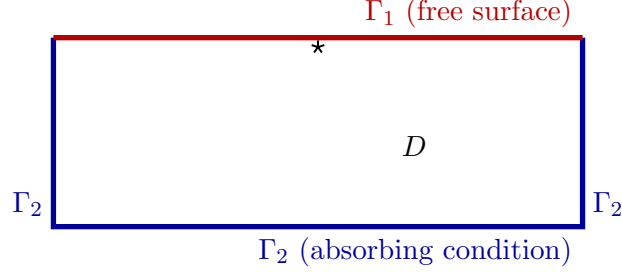


Figure 7: Illustration of domain D : free-surface condition is imposed on the top (red line, Γ_1), while absorbing boundary conditions are imposed elsewhere (blue line, Γ_2). The source (*) is typically positioned near surface.

Upon assuming constant density ρ , Problem (20) can be rewritten as the Helmholtz equation (see Faucher et al. [2020, Remark 1]),

$$-\left(\Delta + \frac{\omega^2}{c(\mathbf{x})^2}\right)p(\mathbf{x}, \omega) = -i\omega\rho f(\mathbf{x}, \omega), \quad (22)$$

where c is the wave speed defined such that

$$c(\mathbf{x}) = \sqrt{\frac{\kappa(\mathbf{x})}{\rho(\mathbf{x})}}. \quad (23)$$

B.2 Dataset

The dataset corresponds to the N couples made up of a wave speed and pressure field, $(c_k, p_k)_{k=1, \dots, N}$, where p_k solves Equation (22) using wave speed c_k . The sources f in Equation (22) is taken a delta-Dirac function δ , and we proceed as follow,

1. Setup the geometrical domain D and configuration (i.e., dimension, frequency for propagation, source position);
2. Create a set of wave speeds that are independent and identically distributed random variables, see Appendix B.3;
3. Solve the wave equation Equation (22) on D for each wave speed c_k . Here, we use a *Hybridizable Discontinuous Galerkin Method* (HDG, Faucher and Scherzer [2020]) for the discretization and (open-source) software **hawen**, see Faucher [2021].
4. Save the resulting pressure field on a Cartesian grid.

We further consider two experiments, each with different size of domain, position of sources, and where we impose different lower and upper bounds for the variation of the wave speeds.

B.3 Generation of Gaussian Random Field wave speeds

We consider realizations of the wave speed c as Gaussian Random Fields (GRF) [Bogachev, 2015, Ghosal and Van der Vaart, 2017, Lord et al., 2014] with Matérn covariance kernel function C_ν such that (see e.g., Lord et al. [2014, Example 7.17])

$$C_\nu(d) = \sigma^2 \frac{2^{1-\nu}}{\Gamma(\nu)} \left(\sqrt{2\nu} \frac{d}{\mathbf{a}} \right)^\nu K_\nu \left(\sqrt{2\nu} \frac{d}{\mathbf{a}} \right). \quad (24)$$

Here, σ is the variance of the process, Γ is the gamma function [Artin, 2015], K_ν is the modified Bessel function of the second kind [Arfken and Weber, 1999, Bowman, 2012], and \mathbf{a} , ν are positive parameters. In particular, ν is known as the *smoothness* of the random field. The distance d/\mathbf{a} between two points $\mathbf{x} = (x_1, \dots, x_n) \in \mathbb{R}^n$ and $\mathbf{x}' = (x'_1, \dots, x'_n) \in \mathbb{R}^n$, is defined such that

$$\frac{d}{\mathbf{a}} := \sqrt{\sum_{i=1}^n \left(\frac{x_i - x'_i}{\lambda_i} \right)^2}, \quad (25)$$

where the vector coefficient $\boldsymbol{\lambda} = (\lambda_1, \dots, \lambda_n)$ defines the correlation length along two points in \mathbb{R}^n . For the computational simulation of the Gaussian process, see [Dietrich and Newsam, 1997] and [Lord et al., 2014]. The wavespeed generation is mainly based in Kumar [2019].

For the following two-dimensional experiments ($n = 2$), we use the following values: $\lambda_1 = \lambda_2 = 0.1$, and the smoothness coefficient is set to be $\nu = 1$.

Remark B.1 (Motivation for GRF wave speeds). The use of Gaussian Random Fields for wave speeds is motivated by the following reasons.

1. GRF realizations result in that $c \in \mathbf{L}^\infty(D; \mathbb{R}^d) \cap \mathbf{L}^2(D; \mathbb{R}^d)$. Therefore, we have a separable Banach space, and it is *legal* to use Neural Operators, or variants, to approximate the map from the wave speed to the pressure field: $c \mapsto p$. For instance, if we were to only have $c \in \mathbf{L}^\infty(D; \mathbb{R}^d)$, the operator would not be covered by the universality in [Kovachki et al., 2021a], as \mathbf{L}^∞ is not a separable Banach space.
2. Using GRF, the dataset comes from a probability distribution on functional space. Therefore, the distribution is independent of the grid resolution, and it allows us to stay in the Statistical Learning framework; allowing us to connect our numerical observations with the theory on functional space.
3. It is easy to draw samples of the GRF, and it has a natural physical interpretation. For instance, in Bayesian statistics, a popular choice of prior probability measures arises from GRF whose covariance kernels are usually related with the Laplace operator or Matérn process (throughout this paper), cf. Nickl and Wang [2020, Section 2.1] and Dashti and Stuart [2017].

B.4 Experimental dataset

We consider two datasets. For the first experiment, we have the following setup:

$$\text{Experiment 1} \left\{ \begin{array}{l} \text{2D domain of size } 3.81 \times 3.81 \text{ km}^2 \\ \text{40 000 GRF wave speeds generated, imposing } 1.5 \text{ km s}^{-1} \leq c(x) \leq 3 \text{ km s}^{-1} \\ \text{The data are } p \text{ that solve Equation (20) at frequency } \omega/(2\pi) = 7 \text{ Hz (one field per wave speed).} \end{array} \right. \quad (26)$$

Both the wave speeds and the pressure field solution are represented on a Cartesian grid of size 128×128 pixels, that is, using a grid step of 30m. We illustrate in Figure 8 a realization of the wave speed model and the corresponding pressure field.

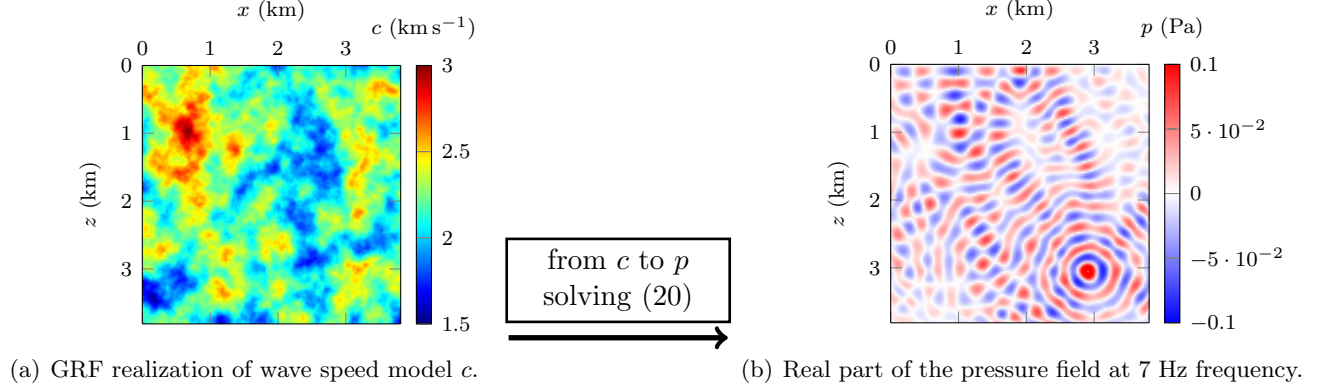


Figure 8: Illustration of the full-wave dataset for Experiment 1 that considers a computational domain of size $3.81 \times 3.81 \text{ km}^2$ with a source buried in the domain. The wave speed and pressure field are represented on a Cartesian grid of size 128×128 with a grid step of 30m. The complete dataset corresponds to 40 000 couples made up of a wave speed model and associated acoustic wave.

For the second experiment, we consider a smaller domain but higher variation of wave speed, and the source is positioned near surface such that:

$$\text{Experiment 2} \left\{ \begin{array}{l} \text{2D domain of size } 1.27 \times 1.27 \text{ km}^2 \\ \text{40 000 GRF wave speeds generated, imposing } 1.5 \text{ km s}^{-1} \leq c(x) \leq 5 \text{ km s}^{-1} \\ \text{The data are } p \text{ that solve Equation (20) at frequency } \omega/(2\pi) = 12 \text{ and } 15 \text{ Hz.} \end{array} \right. \quad (27)$$

Both the wave speeds and the pressure field solution are represented on a Cartesian grid of size 64×64 pixels, that is, using a grid step of 20m. We illustrate in Figure 9 a wave speed model and the corresponding pressure field.

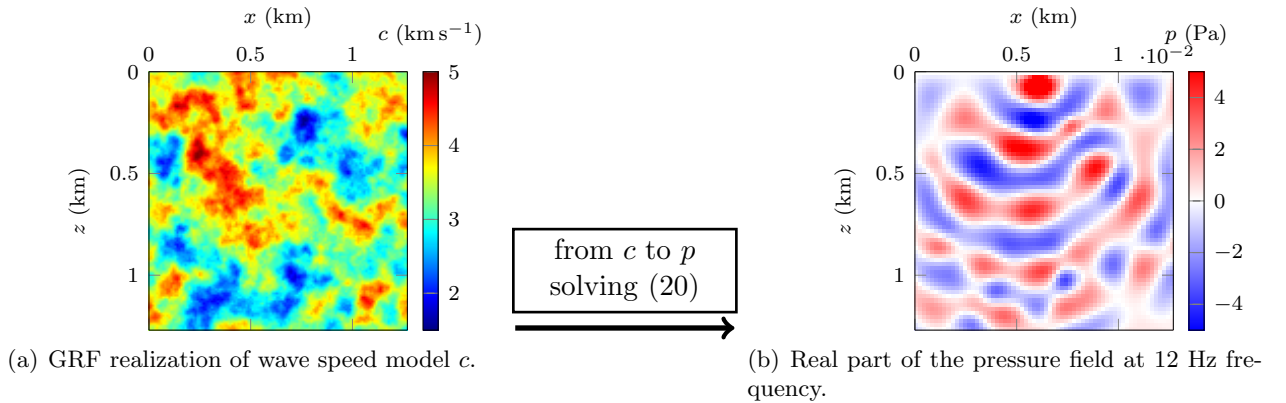


Figure 9: Illustration of the full-wave dataset for Experiment 2 that considers a computational domain of size $1.27 \times 1.27 \text{ km}^2$ with a source near surface. The wave speed and pressure field are represented on a Cartesian grid of size 64×64 with a grid step of 20m. The complete dataset corresponds to 40 000 couples made up of a wave speed model and associated acoustic wave.

C Numerical results of the different neural network architectures

We evaluate the performance of the different architectures using the datasets described in Appendix B, that is, in the context of acoustic wave propagation. For the two experiments we have introduced in Appendix B, we detail the parameters and training used for the different architecture, and show the reconstruction.

C.1 Experiment 1

C.1.1 Parameters of the architectures and training

For Experiment 1 presented Equation (26) and Figure 8, the parameters in the four versions of Neural Operators tested are given Table 2.

	FNO	sNO	(sFNO + ε)v1	(sFNO + ε)v2
Modes	12	12	12	[12, 12, 16, 14]
Layers	4	4	4	[3, 3, 9, 3]
Features	36	36	36	[30, 30, 32, 38]
Activation	GELU	GELU	GELU	GELU
Positional encoder	with grid on $[-1, 1]^2$	with grid on $[-1, 1]^2$	with grid on $[-1, 1]^2$	with grid on $[-1, 1]^2$
Lifting	MLP(ReLU): 3 \rightarrow 18 \rightarrow 36	MLP(ReLU): 3 \rightarrow 18 \rightarrow 36	MLP(ReLU): 3 \rightarrow 18 \rightarrow 36	MLP(ReLU): 3 \rightarrow 18 \rightarrow 36
Projection	MLP (ReLU): 36 \rightarrow 18 \rightarrow 1	MLP(ReLU): 36 \rightarrow 18 \rightarrow 1	MLP(ReLU): 36 \rightarrow 18 \rightarrow 1	MLP(ReLU): 36 \rightarrow 18 \rightarrow 1
Dropout	No	No	No	0.1
Drop Path	No	No	No	0.3

Table 2: **Architectures’ parameters used with the dataset of Experiment 1 (Equation (26) and Figure 8).** All architectures use the same hyperparameters, except for (sFNO + ε) version 2. Following Liu et al. [2022, 2.2 Macrodesign], we have the combination layers=[3, 3, 9, 3] (18 layers), modes=[12, 12, 16, 14], and #features [30, 30, 32, 38]. Interepreted as follows: 3 consecutive layers with 12 modes, and feature space of 30, and so on.

From the results in Experiment 1 Equation (26) the following can be concluded.

1. We do not notice *advantage of using dropout* for 4 layers architectures.
2. We find advantage of using dropout and stochastic depth, whenever the network becomes deep, and overfitting naturally occurs. Besides, we empirically find a major effectiveness of stochastic depth (drop path) [Huang et al., 2016].
3. The stochastic depth in the (sFNO + ε) version 2 increases linearly from 0 in the first layer, to 0.3 in the last.
4. The MLP (local part) of the last three architectures, see Figures 1 and 2 for visualization, is chosen to be a small MLP.

Mapping:

$$\#feature \rightarrow 4(\#feature) \rightarrow \#feature.$$

We keep the inverse bottleneck tradition in Transformers, and Liu et al. [2022, 2.4], popularized in Sandler et al. [2018].

C.1.2 Training of Experiment 1

The training uses the following components:

1. For all the architectures we use Adam Optimizer [Kingma and Ba, 2014], with an initial learning rate 10^{-3} , with a StepLR scheduler with parameters: step size=80, and a multiplicative factor of learning rate decay of $\gamma = 0.5$.
2. The number of epochs is chosen to 100 for the first 3 architectures (FNO, sFNO and (sFNO + ε) version 1). For the last, (sFNO + ε) version 2, it is extended to 200 (the main purpose is to push the architecture as much as possible, and follows some of the training recipes in Transformers and ConvNeXt).
3. In all the architectures, we use a small ℓ_2 -weight regularizer with parameter 10^{-5} .
4. The training is implemented with 25000 of 30000, the testing is make with 5000.

C.1.3 Results of Experiment 1

Following training using couples made up of wave speeds and pressure fields described Appendix B, the objective of the network is to predict a pressure field given a GRF realization of wave speed. In Figure 10, we show the results for three realizations of wave speeds in the context of Experiment 1. The norms of the relative difference with the reference solution (obtained from the discretization of the PDE) for 6 realizations are given Table 3.

GRF Realization	FNO	sFNO	(sFNO + ε)v1	(sFNO + ε)v2
1	0.4030	0.2788	0.2419	0.0869
2	0.4155	0.2703	0.2477	0.0993
3	0.4548	0.2980	0.2414	0.0902
4	0.4396	0.2855	0.2453	0.0810
5	0.4325	0.2768	0.2442	0.0849
6	0.4301	0.2800	0.2538	0.0877

Table 3: **Norm of the relative L_2 -norm for Experiment 1 Equation (26).** Multiple realization of the trained networks with different random seed. Each row represent a different realization, and the values corresponds to the test loss of the architectures after training. The visualization of the table is presented in the main section of the paper, Figure 4.

We see that the reconstructions using FNO are the least accurate and do not fully capture the interference patterns of waves, in all three cases pictures in Figure 11. The results obtained with architectures (sFNO + ε)v1 and sFNO are relatively closed, even though (sFNO + ε)v1 appears slightly more accurate in terms of relative error. Architecture (sFNO + ε)v2, that uses more layers, is the most accurate with relative error of about one order of magnitude less than the others.

C.2 Experiment 2

C.2.1 Parameters of the architectures and training

For Experiment 2 presented Equation (27) and Figure 9, the parameters in the four versions of Neural Operators tested are given Table 4. In this experiment, we further compare two frequencies for the wave propagation with $\omega/(2\pi)$ set to 12 and 15 Hz for Equation (20).

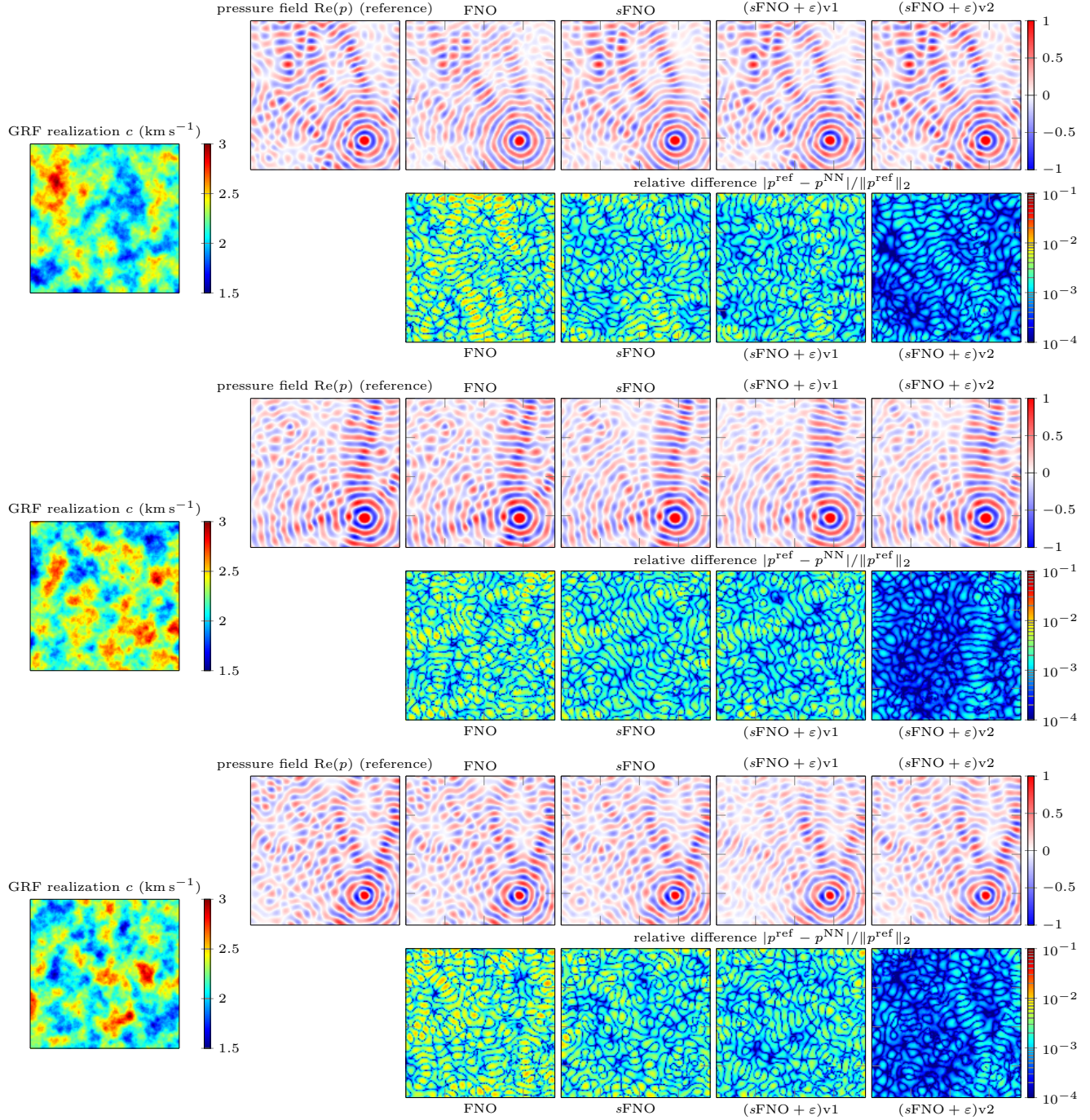


Figure 10: Pressure field reconstructed for Experiment 1 (Equation (26) and Figure 8) with the different architectures for three test-cases. *First column* shows independent GRF realization of the wave speed (see Appendix B). *Second column* shows the solution of the wave PDE obtained with software `hawen` [Faucher, 2021], which we consider as the *reference solution*, see Appendix B. *Other columns* show the approximated reconstruction using the different architectures: *FNO*, see Kovachki et al. [2021b]; sequential structure (*sFNO*, see Section 2.2); and the solutions provided by *sFNO + ε*, Section 2.3. In each case, we show the real part of the pressure field, and the relative error with the reference solution using a logarithmic scale.

C.2.2 Training of Experiment 2

The training uses the following components:

	FNO	sFNO	(sFNO + ε)v1	(sFNO + ε)v2
Modes	12	12	12	[12, 12, 16, 14]
Layers	4	4	4	[3, 3, 9, 3]
Features	36	36	36	[30, 30, 32, 38]
Activation	GELU	GELU	GELU	GELU
Positional encoder	with grid on $[-1, 1]^2$	with grid on $[-1, 1]^2$	with grid on $[-1, 1]^2$	with grid on $[-1, 1]^2$
Lifting	MLP(ReLU): $3 \rightarrow 18 \rightarrow 36$	MLP(ReLU): $3 \rightarrow 18 \rightarrow 36$	MLP(ReLU): $3 \rightarrow 18 \rightarrow 36$	MLP(ReLU): $3 \rightarrow 18 \rightarrow 36$
Projection	MLP (Id): $36 \rightarrow 1$	MLP(Id): $36 \rightarrow 2$	MLP(Id): $36 \rightarrow 2$	MLP(Id): $36 \rightarrow 2$
Dropout	No	No	No	0.1
Drop Path	No	No	No	0.3

Table 4: **Architectures’ parameters 12 Hz and 15 Hz.** The only architecture that differs is (sFNO + ε) version 2 similarly than Experiment 1. Furthermore, there are two differences with respect to Table 4, (a) the networks recovered both real, and imaginary part of the pressure field in the time-harmonic wave equation, i.e., the output is a vector field in \mathbb{R}^2 which can be associated with \mathbb{C} , and (b) the projection operator is simplified by a linear layer instead of a MLP to speed up the training process.

1. For all the architectures we use Adam Optimizer [Kingma and Ba, 2014], with an initial learning rate 10^{-3} , with a StepLR scheduler with parameters: step size=80, and a multiplicative factor of learning rate decay of $\gamma = 0.5$.
2. The number of epochs is chosen to 100 for the first 3 architectures (FNO, sFNO and sFNO + ε) version 1). For the last, (sFNO + ε) version 2, it is extended to 200 (the main purpose is to push the architecture as much as possible, and follows some of the training recipes in Transformers and ConvNeXt).
3. In all the architectures, we use a small ℓ_2 -weight regularizer with parameter 10^{-5} .
4. The training is implemented with 25000 of 50000, validation with 5000 generated samples, the testing is make with 25000.

C.2.3 Results of Experiment 2

In Figures 11 and 12, we show the results for three realization of wave speeds in the context of Experiment 2, respectively for frequency $\omega/(2\pi)$ set to 12 and 15 Hz.

We see that the best reconstructions are obtained using architecture (sFNO + ε)v2, which is expected as it uses multiple layers. The reconstruction with FNO is less accurate than the other, and we observe that (sFNO + ε)v1 is slightly more accurate than the architecture sFNO in all cases. Comparing the frequencies, it appears that higher frequencies (15 Hz in Figure 12 compared to 12 Hz in Figure 11) are slightly harder to reconstruct. This can be explained as the wavelength becomes smaller, hence more oscillations and features have to be anticipated by the networks. The results of Experiments 2 are totally consistent with Experiment 1 of Figure 10. Consequently, we see that the approach is robust with respect to the change in the the position of the source, the size of the domain, variation of wave speeds, and change of frequencies.

C.2.4 Comparison of the Experiment 2 (multiple random initializations)

We randomly initialize the architectures, and we generate the equivalent diagram of Figure 4 at higher frequencies $\omega/(2\pi) = 12, 15$ Hz. The results are consistent with the behavior in Figure 4, throughout multiple realizations of the networks’ parameters and training paths. It should be noticed that the behavior is more pronounced at higher frequencies. Showing the advantages of the network’s modifications.

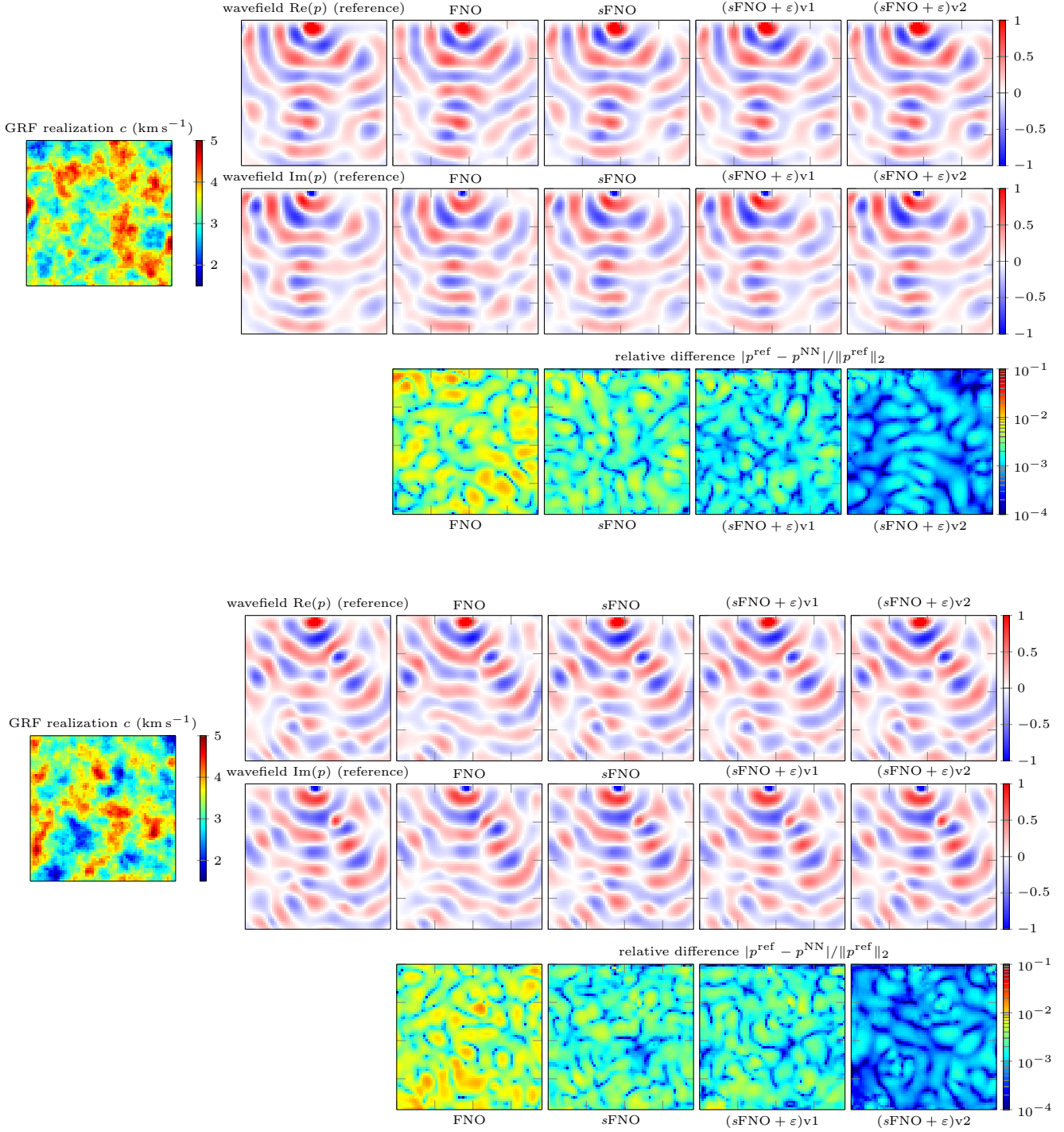


Figure 11: Pressure field (12 Hz) reconstructed for Experiment 2 (Equation (27) and Figure 9) at frequency 12 Hz with the different architectures for two GRF realizations of the wave speed. *Left column* shows independent GRF realization of the wave speed (see Appendix B). *Second column* shows the real and imaginary part of the pressure field solution to the wave PDE at frequency 12 Hz, obtained with software `hawen` [Faucher, 2021], which we consider as the *reference solution*, see Appendix B. *Other columns* show the approximated reconstructions using the different architectures: *FNO*, see Kovachki et al. [2021b]; sequential structure (*sFNO*, see Section 2.2); and the solutions provided by *sFNO* + ε , Section 2.3. In each case, we show the real and imaginary parts of the pressure fields, and the relative error with the reference solution on a logarithmic scale.

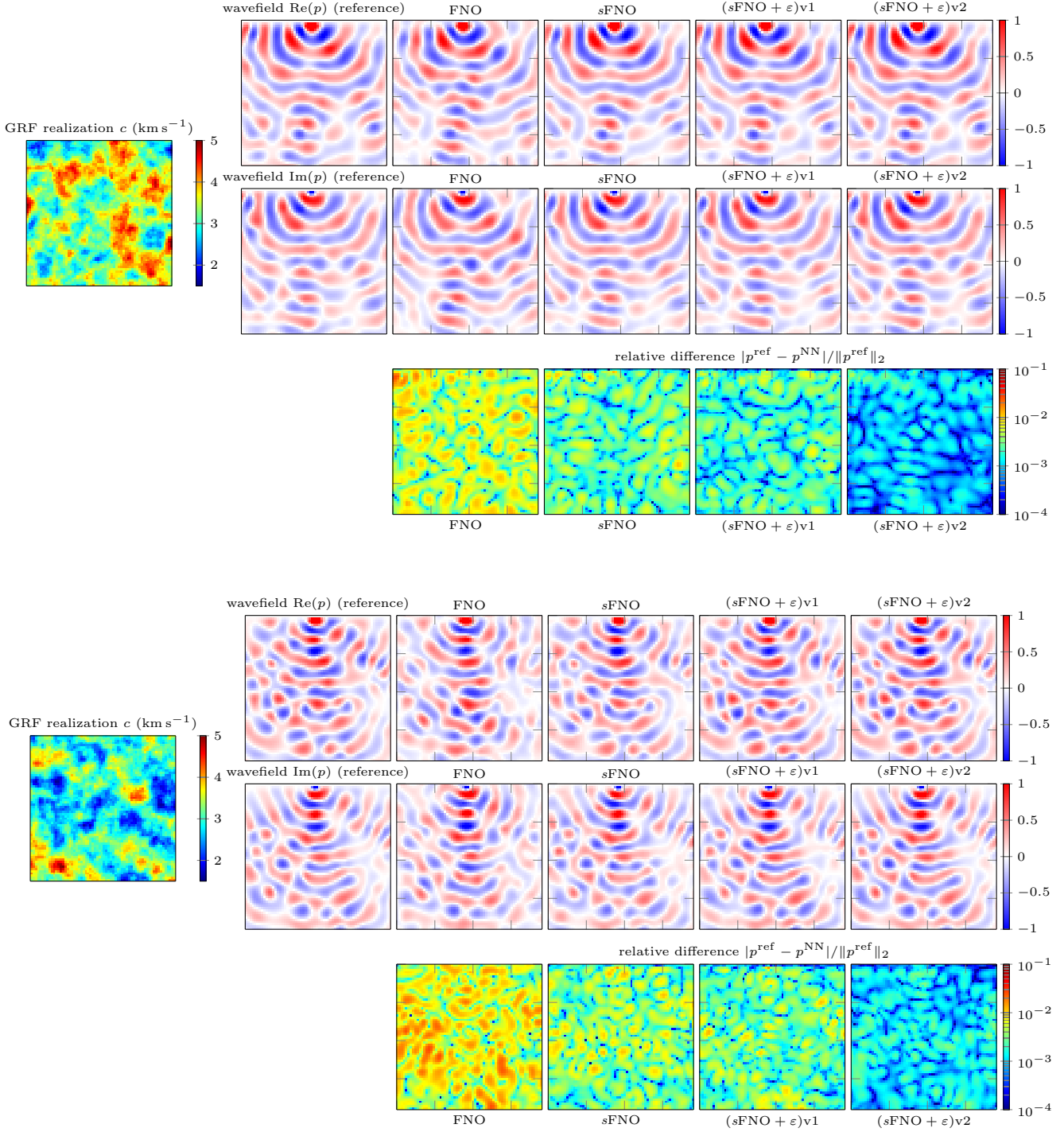


Figure 12: Pressure field (15 Hz) reconstructed for Experiment 2 (Equation (27) and Figure 9) at frequency 15 Hz with the different architectures for two GRF realizations of the wave speed. *Left column* shows independent GRF realization of the wave speed (see Appendix B). *Second column* shows the real and imaginary part of the pressure field solution to the wave PDE at frequency 12 Hz, obtained with software `hawen` [Faucher, 2021], which we consider as the *reference solution*, see Appendix B. *Other columns* show the approximated reconstructions using the different architectures: *FNO*, see Kovachki et al. [2021b]; sequential structure (*sFNO*, see Section 2.2); and the solutions provided by *sFNO* + ϵ , Section 2.3. In each case, we show the real and imaginary parts of the pressure fields, and the relative error with the reference solution on a logarithmic scale.

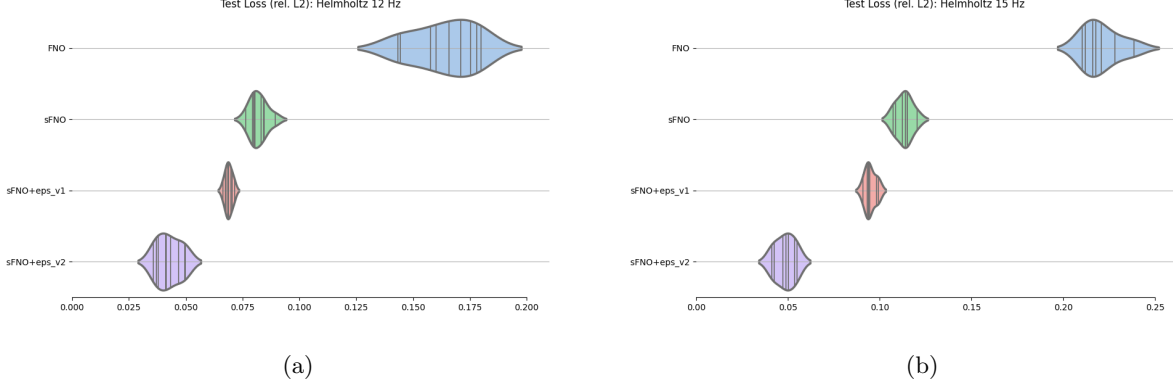


Figure 13: **Comparison of test-loss for the Experiment 2, Equation Appendix B.** (a) $\omega/(2\pi) = 12$ Hz, and each architecture is trained 9 times (b) $\omega/(2\pi) = 12$ Hz each architecture is trained 8 times. The relative L^2 -loss, $\|\mathcal{G}^{\text{ref}} - \mathcal{G}^{\text{approx}}\|_{L^2} / \|\mathcal{G}^{\text{ref}}\|_{L^2}$ in the test data is shown, as Figure 4.

C.3 Visualization of the loss landscape of all the architectures (Experiment 1 data).

The significant performance differences observed between the considered architectures prompted us to investigate their respective loss landscapes. For that purpose, we used the loss landscape visualization method proposed by Li et al. [2018a] and its open-source implementation Li et al. [2018b]. This approach’s basic idea consists of computing the principal components of the weights associated with each model obtained during training. In particular, the first two principal components span a two-dimensional domain that can be sampled to yield a loss surface centered around the optimized model. While this transformation amounts to a dramatic linear dimensionality reduction, it has been shown to offer valuable insight into important qualitative differences between architectures [Li et al., 2018a].

Figure 14 shows two-dimensional and three-dimensional views of the loss landscapes corresponding to the FNO, sFNO, and sFNO + ε architectures. Note that all visualizations use identical scaling factors and color scales to facilitate comparisons. Similarly, the level sets correspond to the same set of loss values.

These results allow us to make several observations. First, the FNO loss landscape exhibits much higher curvature than the other two architectures, which are both fairly flat in the vicinity of the found loss minimizer. Qualitatively, however, all landscapes exhibit the same pair of neighboring minima with a separating saddle point, which creates a curved loss valley. Further, the trajectories are surprisingly similar across architectures. In each case, the SGD-based optimization (Adam) procedures crossed the first minimum’s basin before entering the second lower basin. Hence, the main difference between these different landscapes to explain the superior performance of sFNO + ε appears to boil down to the depth of their respective loss minimum.

To further investigate the observed similarities between training trajectories, we decided to compare them across additional PCA dimensions. The corresponding results are shown in a scatterplot matrix in Figure 15.

Note that the orientations of the principal components were matched using a simple geometric correlation criterion to facilitate comparison. This visualization confirms the remarkable qualitative similarities between the different architectures’ learning trajectories. Nonetheless, these similarities decrease in higher dimensions. A possible interpretation of these observations is that the very low-dimensional nature of the parameter subspace in which the comparison is performed is too low to allow for a more insightful comparison between architectures. Alternatively, the linear nature of the dimensionality reduction may obfuscate the existence of a low-dimensional, nonlinear training trajectory manifold that more effectively captures the training dynamic. We intend to explore both avenues in future work.

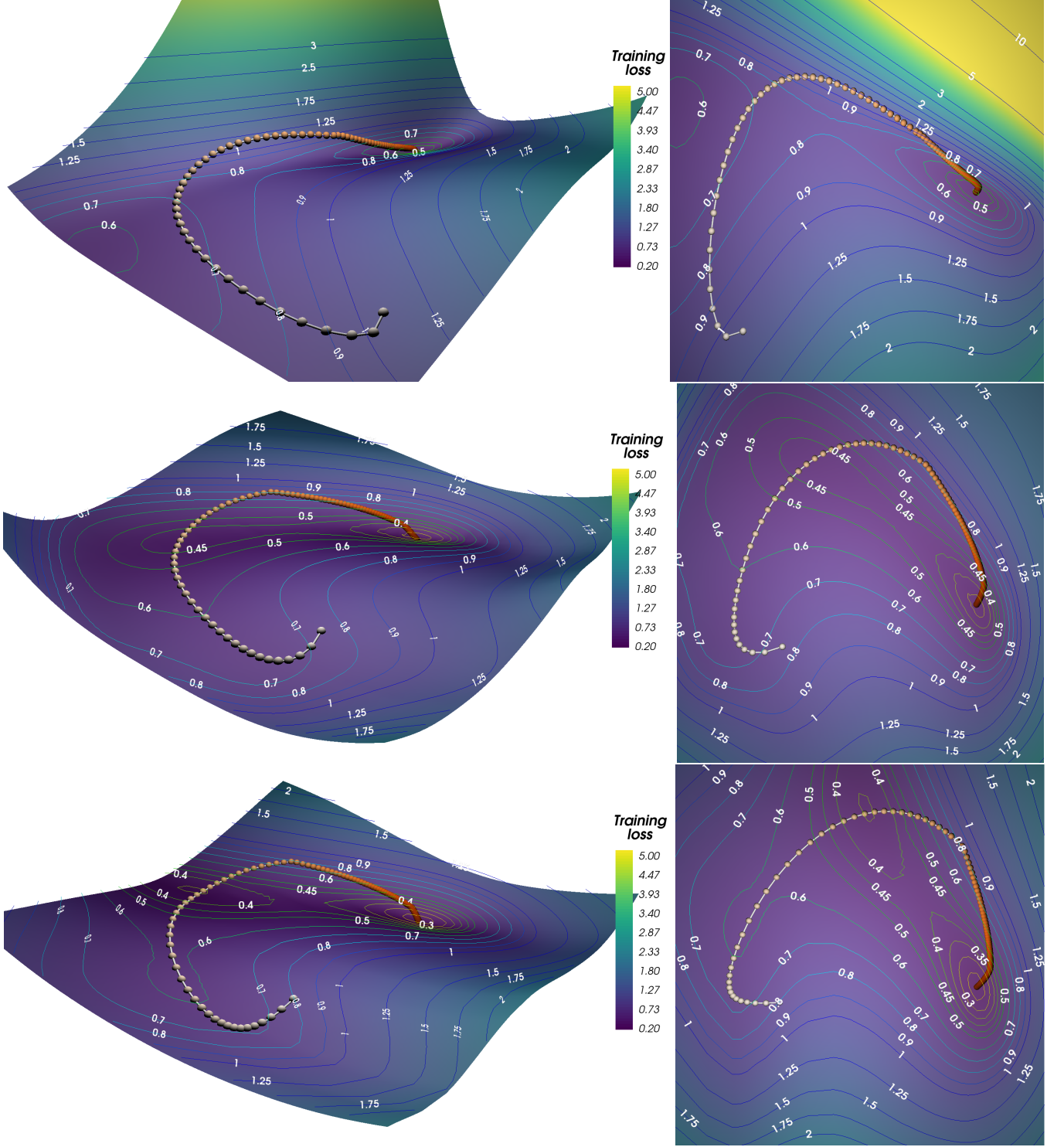


Figure 14: Loss landscapes of the considered architectures. Top: FNO, center: sFNO, bottom: sFNO + ε version 1

D Proof of Lemma 4.2

Lemma D.1 (Lemma 4.2). *Let Assumption 4.1 holds. Let suppose there exists $R > 0$ such that*

$$\|\mathcal{G}(a)\|_{\mathbf{L}^2(D; \mathbb{R}^{d_u})} \leq R, \quad \forall \mathcal{G} \in \mathcal{G}, \quad a \in \text{supp}(\mu_a). \quad (28)$$

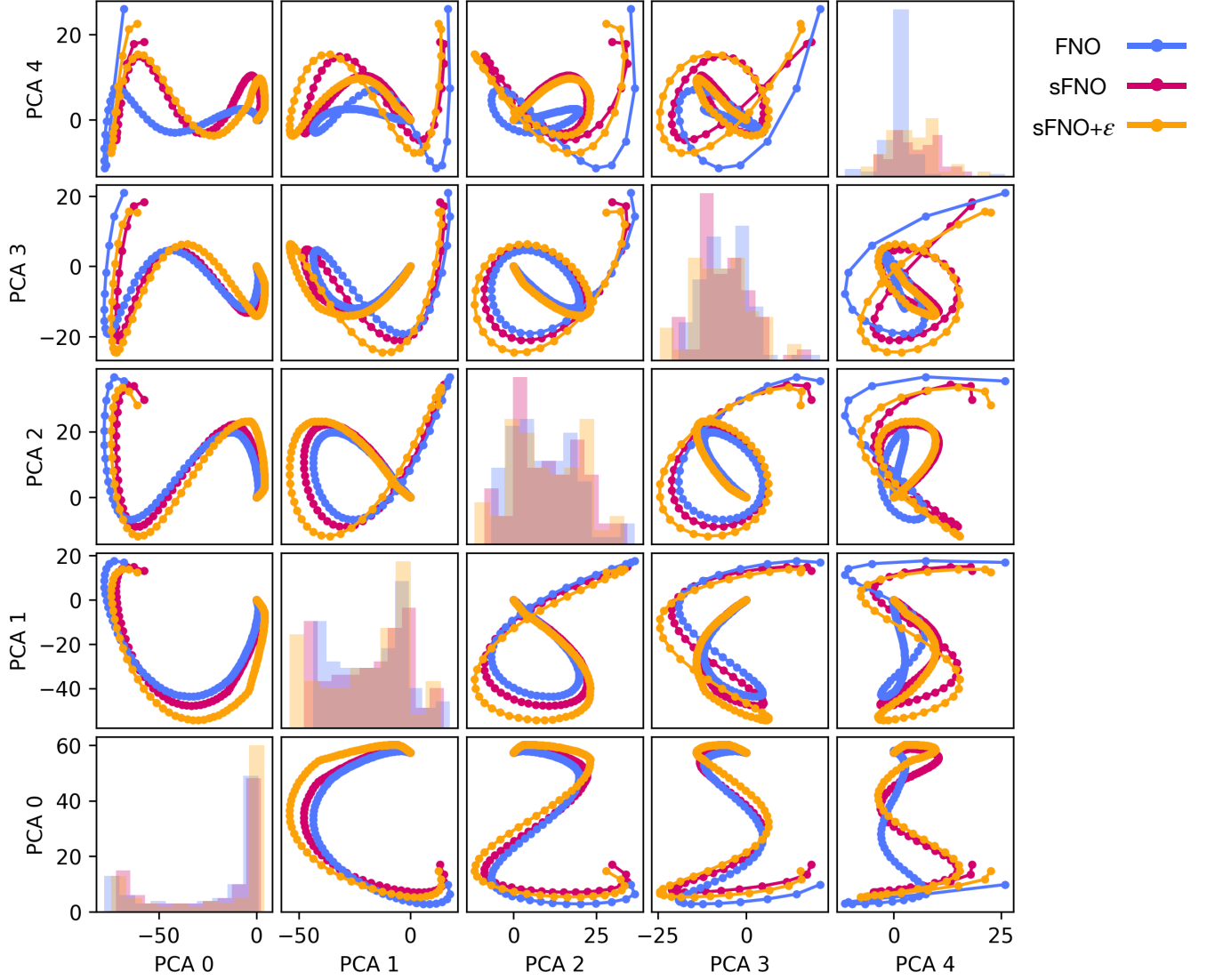


Figure 15: Visual comparison of learning trajectories in PCA coordinates for FNO, sFNO, and sFNO + ε architectures. The first five principal components are considered.

for the Hypothesis class, \mathcal{G} . Hence, for any $\delta > \log 2$, the following inequality holds with probability greater than $1 - 2\exp(-\delta)$,

$$\mathcal{L}(\mathcal{G}) \leq \widehat{\mathcal{L}}_{\mathcal{S}}(\mathcal{G}) + 2\mathfrak{R}_{\mathcal{S}}(\mathcal{F}_{\mathcal{G}}) + (\rho R + R_u) \sqrt{\frac{2\delta}{n}}, \quad \forall \mathcal{G} \in \mathcal{G}, \quad (29)$$

where $\mathcal{F}_{\mathcal{G}} := \{(a, u) \mapsto \ell(\mathcal{G}(a), u) : (a, u) \in \text{supp}(\mu), \mathcal{G} \in \mathcal{G}\}$, and $\mathfrak{R}_{\mathcal{S}}(\mathcal{F}_{\mathcal{G}})$ is the (empirical) Rademacher Complexity of the class $\mathcal{F}_{\mathcal{G}}$, see Definition A.10.

Proof. By using (28), we have for $f = \ell(\mathcal{G}(\cdot), \cdot) \in \mathcal{F}_{\mathcal{G}}$ and $\mathcal{G} \in \mathcal{G}$,

$$\begin{aligned} |f(a, u)| &\leq |\ell(\mathcal{G}(a), u) - \ell(0, u)| + |\ell(0, u)| \\ &\stackrel{\text{Assumption 4.1(i)(ii)}}{\leq} \rho \|\mathcal{G}(a)\|_{\mathbf{L}^2(D; \mathbb{R}^{d_u})} + R_u \leq \rho R + R_u, \end{aligned}$$

for $(a, u) \in \mathbf{L}^2(D; \mathbb{R}^{d_a}) \times \mathbf{L}^2(D; \mathbb{R}^{d_u})$, which implies that by employing Theorem 4.10 in Wainwright [2019] or Theorem 3.4.5 in Giné and Nickl [2015], we have the following inequality with probability greater than

$$1 - 2e^{-\delta},$$

$$\begin{aligned} |\mathcal{L}(\mathcal{G}) - \widehat{\mathcal{L}}_S(\mathcal{G})| &\leq \sup_{f \in \mathcal{F}_{\mathcal{G}}} \left| \frac{1}{n} \sum_{i=1}^n f(a_i, u_i) - E_{(a,u) \sim \mu}[f(a, u)] \right| \\ &\leq 2E \left[\sup_{f \in \mathcal{F}_{\mathcal{G}}} \frac{1}{n} \left| \sum_{i=1}^n \epsilon_i f(a_i, u_i) \right| \right] + (\rho R + R_u) \sqrt{\frac{2\delta}{n}}, \quad \mathcal{G} \in \mathcal{G}, \end{aligned}$$

where $\{\epsilon_i\}_{i=1}^n$ is a sequence of i.i.d. RV's with Rademacher distribution; i.e., $\mathbf{P}\{\epsilon_i = 1\} = 1/2 = \mathbf{P}\{\epsilon_i = -1\}$. \square

E Proof of Theorem 4.4

Theorem E.1 (Theorem 4.4). *Let suppose Assumptions 4.1 and 4.3 hold. Then,*

$$\mathfrak{R}_S(\mathcal{F}_{\mathcal{N}}) \leq \gamma L^{\frac{\hat{d}+2}{\hat{d}+1}} \{(C_w + C_k)C_\sigma\}^L \left(\frac{1}{n}\right)^{\frac{1}{\hat{d}+1}}, \quad (30)$$

where $\hat{d} := \text{ddim}(D \times D)$ is the doubling number of $D \times D$, and γ is the positive constant independent of L and n , defined in 45.

Proof. By employing Theorem 1.1 in Kakade and Tewari [2008], we have

$$\mathfrak{R}_S(\mathcal{F}_{\mathcal{N}}) \leq \inf_{\alpha \geq 0} \left\{ 4\alpha + \frac{12}{\sqrt{n}} \int_{\alpha}^{\infty} (\log N(\varepsilon, \mathcal{F}_{\mathcal{N}}, \|\cdot\|_S))^{\frac{1}{2}} d\varepsilon \right\} \quad (31)$$

where $\|f\|_S := (\frac{1}{n} \sum_{i=1}^n f(a_i, u_i)^2)^{\frac{1}{2}}$. Here, we denote by $N(\varepsilon, \mathcal{F}, \|\cdot\|)$ the covering number of the function space \mathcal{F} which means the minimal cardinality of a subset $C \subset \mathcal{F}$ that covers \mathcal{F} at scale ε with respect to the norm $\|\cdot\|$. In the following, we will estimate the covering number $N(\varepsilon, \mathcal{F}_{\mathcal{N}}, \|\cdot\|_S)$.

Let $f = \ell(\mathcal{G}(\cdot), \cdot)$ and $f' = \ell(\mathcal{G}'(\cdot), \cdot)$ where $\mathcal{G}, \mathcal{G}' \in \mathcal{N}$. By (i) of Assumption 4.1, we calculate

$$|f(a, u) - f'(a, u)| = |\ell(\mathcal{G}(a), u) - \ell(\mathcal{G}'(a), u)| \leq \rho \|\mathcal{G}(a) - \mathcal{G}'(a)\|_{\mathbf{L}^2(D; \mathbb{R}^{d_u})}. \quad (32)$$

Denoting by

$$\begin{aligned} \mathcal{G}_\ell &:= (W_\ell + \mathcal{K}_\ell) \circ \sigma(W_{\ell-1} + \mathcal{K}_{\ell-1}) \circ \cdots \circ \sigma(W_0 + \mathcal{K}_0), \\ \mathcal{G}'_\ell &:= (W'_\ell + \mathcal{K}'_\ell) \circ \sigma(W'_{\ell-1} + \mathcal{K}'_{\ell-1}) \circ \cdots \circ \sigma(W'_0 + \mathcal{K}'_0), \end{aligned}$$

the quantity $\|\mathcal{G}(a) - \mathcal{G}'(a)\|_{\mathbf{L}^2(D; \mathbb{R}^{d_u})}$ is evaluated by

$$\begin{aligned} \|\mathcal{G}(a) - \mathcal{G}'(a)\|_{\mathbf{L}^2(D; \mathbb{R}^{d_u})} &= \|\mathcal{G}_L(a) - \mathcal{G}'_L(a)\|_{\mathbf{L}^2(D; \mathbb{R}^{d_{L+1}})} \\ &= \left\| (W_L + \mathcal{K}_L) \circ \sigma(\mathcal{G}_{L-1}(a)) - (W_L + \mathcal{K}_L) \circ \sigma(\mathcal{G}'_{L-1}(a)) \right. \\ &\quad \left. + (W_L + \mathcal{K}_L) \circ \sigma(\mathcal{G}'_{L-1}(a)) - (W'_L + \mathcal{K}'_L) \circ \sigma(\mathcal{G}'_{L-1}(a)) \right\|_{\mathbf{L}^2(D; \mathbb{R}^{d_{L+1}})} \\ &\stackrel{\text{Assumption 4.3(v)}}{\leq} \left(\underbrace{\|W_L\|_{\text{op}}}_{\leq C_w} + \underbrace{\|\mathcal{K}_L\|_{\text{op}}}_{\leq C_k} \right) C_\sigma \|\mathcal{G}_{L-1}(a) - \mathcal{G}'_{L-1}(a)\|_{\mathbf{L}^2(D; \mathbb{R}^{d_L})} \\ &\quad + \left(\|W_L - W'_L\|_{\text{op}} + \|\mathcal{K}_L - \mathcal{K}'_L\|_{\text{op}} \right) C_\sigma \|\mathcal{G}'_{L-1}(a)\|_{\mathbf{L}^2(D; \mathbb{R}^{d_L})}, \end{aligned} \quad (33)$$

where $\|\cdot\|_{\text{op}}$ is the Operator norm. Here, we have employed the following estimations:

$$\|W_L g\|_{\mathbf{L}^2(D; \mathbb{R}^{d_{L+1}})}^2 \leq \int_D \underbrace{\|W_L g(x)\|_2^2}_{\leq \|W_L\|_{\mathbb{F}}^2 \|g(x)\|_2^2} dx \stackrel{\text{Assumption 4.3(i)}}{\leq} C_w^2 \|g\|_{\mathbf{L}^2(D; \mathbb{R}^{d_L})}^2, \quad (34)$$

$$\begin{aligned} \|\mathcal{K}_L g\|_{\mathbf{L}^2(D; \mathbb{R}^{d_{L+1}})}^2 &\leq \int_D \left\| \int_D \mathcal{K}_L(x, y) g(y) dy \right\|_2^2 dx \leq |D|^2 \|k_L\|_{\mathbb{F}, \infty}^2 \|g\|_{\mathbf{L}^2(D; \mathbb{R}^{d_L})}^2 \\ &\stackrel{\leq |D| \int_D \|\mathcal{K}_L(x, y)\|_{\mathbb{F}}^2 \|g(y)\|_2^2 dy}{\leq} \\ &\stackrel{\text{Assumption 4.3(ii)}}{\leq} C_k^2 \|g\|_{\mathbf{L}^2(D; \mathbb{R}^{d_L})}^2, \end{aligned} \quad (35)$$

for $g \in \mathbf{L}^2(D; \mathbb{R}^{d_L})$, where $\|\cdot\|_2$ is the ℓ_2 -norm. By the same argument in (33)–(35), we evaluate

$$\begin{aligned} &\|\mathcal{G}_{L-1}(a) - \mathcal{G}'_{L-1}(a)\|_{\mathbf{L}^2(D; \mathbb{R}^{d_L})} \\ &\leq (C_w + C_k) C_\sigma \|\mathcal{G}_{L-2}(a) - \mathcal{G}'_{L-2}(a)\|_{\mathbf{L}^2(D; \mathbb{R}^{d_{L-1}})} \\ &+ \left(\|W_{L-1} - W'_{L-1}\|_{\text{op}} + \|\mathcal{K}_{L-1} - \mathcal{K}'_{L-1}\|_{\text{op}} \right) C_\sigma \|\mathcal{G}_{L-2}(a)\|_{\mathbf{L}^2(D; \mathbb{R}^{d_{L-1}})}. \end{aligned} \quad (36)$$

By repeatedly evaluating $\|\mathcal{G}_\ell(a) - \mathcal{G}'_\ell(a)\|_{\mathbf{L}^2(D; \mathbb{R}^{d_{\ell+1}})}$ ($\ell = L, L-1, \dots, 0$), we obtain

$$\begin{aligned} &\|\mathcal{G}(a) - \mathcal{G}'(a)\|_{\mathbf{L}^2(D; \mathbb{R}^{d_u})} \\ &\leq \{(C_w + C_k) C_\sigma\}^L \underbrace{\|(W_0 + \mathcal{K}_0)(a) - (W'_0 + \mathcal{K}'_0)(a)\|_{\mathbf{L}^2(D; \mathbb{R}^{d_1})}}_{\stackrel{\text{Assumption 4.3(iii)}}{\leq} C_a (\|W_0 - W'_0\|_{\text{op}} + \|\mathcal{K}_0 - \mathcal{K}'_0\|_{\text{op}})} \\ &+ \sum_{\ell=0}^{L-1} \left(\|W_{\ell+1} - W'_{\ell+1}\|_{\text{op}} + \|\mathcal{K}_{\ell+1} - \mathcal{K}'_{\ell+1}\|_{\text{op}} \right) \\ &\quad \times \underbrace{(C_w + C_k)^{L-1-\ell} C_\sigma^{L-\ell} \|\mathcal{G}'_\ell(a)\|_{\mathbf{L}^2(D; \mathbb{R}^{d_{\ell+1}})}}_{\stackrel{(38)}{\leq} \{(C_w + C_k) C_\sigma\}^L C_a} \\ &\leq \{(C_w + C_k) C_\sigma\}^L C_a \sum_{\ell=0}^L \left(\|W_\ell - W'_\ell\|_{\text{op}} + \|\mathcal{K}_\ell - \mathcal{K}'_\ell\|_{\text{op}} \right). \end{aligned} \quad (37)$$

Here, we have employed the following estimation:

$$\|\mathcal{G}'_\ell\|_{\mathbf{L}^2(D; \mathbb{R}^{d_{\ell+1}})}^2 \leq (C_w + C_k)^{\ell+1} C_\sigma^\ell C_a. \quad (38)$$

Furthermore, by using ideas of (34) and (35), we estimate

$$\begin{aligned} \|W_\ell - W'_\ell\|_{\text{op}} &\leq \|W_\ell - W'_\ell\|_{\mathbb{F}} \\ &\leq \sum_{j=1}^{d_{\ell+1}} \sum_{i=1}^{d_\ell} |w_{\ell, ij} - w'_{\ell, ij}| \leq \sum_{j=1}^{d_{\ell+1}} \sum_{i=1}^{d_\ell} C_w \left| \frac{w_{\ell, ij}}{C_w} - \frac{w'_{\ell, ij}}{C_w} \right|, \end{aligned} \quad (39)$$

$$\begin{aligned} \|\mathcal{K}_\ell - \mathcal{K}'_\ell\|_{\text{op}} &\leq |D| \|k_\ell - k'_\ell\|_{\mathbb{F}, \infty} \\ &\leq \sum_{j=1}^{d_{\ell+1}} \sum_{i=1}^{d_\ell} |D| \|k_{\ell, ij} - k'_{\ell, ij}\|_{\mathbf{L}^\infty(D \times D; \mathbb{R})} \leq \sum_{j=1}^{d_{\ell+1}} \sum_{i=1}^{d_\ell} C_k \left\| \frac{k_{\ell, ij}}{C_k/|D|} - \frac{k'_{\ell, ij}}{C_k/|D|} \right\|_{\mathbf{L}^\infty(D \times D; \mathbb{R})}. \end{aligned} \quad (40)$$

Combining (32), (37), (39), and (40), the norm $\|f - f'\|_{\mathcal{S}}$ is estimated by

$$\begin{aligned} \|f - f'\|_{\mathcal{S}} &= \left(\frac{1}{n} \sum_{i=1}^n |f(a_i, u_i) - f'(a_i, u_i)|^2 \right)^{\frac{1}{2}} \\ &\leq \sum_{\ell=0}^L \sum_{j=1}^{d_{\ell+1}} \sum_{i=1}^{d_{\ell}} \left[\rho \{ (C_w + C_k) C_{\sigma} \}^L C_a C_w \left| \frac{w_{\ell,ij}}{C_w} - \frac{w'_{\ell,ij}}{C_w} \right| \right. \\ &\quad \left. + \rho \{ (C_w + C_k) C_{\sigma} \}^L C_a C_k \left\| \frac{k_{\ell,ij}}{C_k/|D|} - \frac{k'_{\ell,ij}}{C_k/|D|} \right\|_{\mathbf{L}^{\infty}(D \times D; \mathbb{R})} \right], \end{aligned}$$

which implies that we have

$$\begin{aligned} &N(\varepsilon, \mathcal{F}_{\mathcal{N}}, \|\cdot\|_{\mathcal{S}}) \\ &\leq \prod_{\ell=0}^L \prod_{j=1}^{d_{\ell+1}} \prod_{i=1}^{d_{\ell}} N \left(\frac{\varepsilon}{2 \left(\sum_{\ell=0}^L d_{\ell} d_{\ell+1} \right) \rho \{ (C_w + C_k) C_{\sigma} \}^L C_a C_w}, [-1, 1], |\cdot| \right) \\ &\times N \left(\frac{\varepsilon}{2 \left(\sum_{\ell=0}^L d_{\ell} d_{\ell+1} \right) \rho \{ (C_w + C_k) C_{\sigma} \}^L C_a C_k}, \mathcal{F}_{C_{\beta}}, \|\cdot\|_{\mathbf{L}^{\infty}(D \times D; \mathbb{R})} \right), \end{aligned} \quad (41)$$

where $\mathcal{F}_{C_{\beta}} := \{k : D \times D \rightarrow [-1, 1] \mid k \text{ is } C_{\beta} - \text{Lipschitz}\}$ (see (v) in Assumption 4.3).

By taking logarithmic functions in (41), we have

$$\begin{aligned} &\log N(\varepsilon, \mathcal{F}_{\mathcal{N}}, \|\cdot\|_{\mathcal{S}}) \\ &\leq \left(\sum_{\ell=0}^L d_{\ell} d_{\ell+1} \right) \left\{ \underbrace{\log N \left(\frac{\varepsilon}{2 \left(\sum_{\ell=0}^L d_{\ell} d_{\ell+1} \right) \rho \{ (C_w + C_k) C_{\sigma} \}^L C_a C_w}, [-1, 1], |\cdot| \right)}_{=: H_w(\varepsilon)} \right. \\ &\quad \left. + \underbrace{\log N \left(\frac{\varepsilon}{2 \left(\sum_{\ell=0}^L d_{\ell} d_{\ell+1} \right) \rho \{ (C_w + C_k) C_{\sigma} \}^L C_a C_k}, \mathcal{F}_{C_{\beta}}, \|\cdot\|_{\mathbf{L}^{\infty}(D \times D; \mathbb{R})} \right)}_{=: H_k(\varepsilon)} \right\}. \end{aligned} \quad (42)$$

By using Example 5.3 of Wainwright [2019] and Lemma 4.2 of Gottlieb et al. [2016], we estimate H_w and H_k , respectively as follows:

$$\begin{aligned} H_w(\varepsilon) &\leq \log \left(1 + \frac{2 \left(\sum_{\ell=0}^L d_{\ell} d_{\ell+1} \right) \rho \{ (C_w + C_k) C_{\sigma} \}^L C_a C_w}{\varepsilon} \right) \\ &\leq \left(\frac{I_w}{\varepsilon} \right) \leq \left(\frac{I_w}{\varepsilon} \right)^{\hat{d}+1}, \quad \text{for } 0 < \varepsilon < 2 \left(\sum_{\ell=0}^L d_{\ell} d_{\ell+1} \right) \rho \{ (C_w + C_k) C_{\sigma} \}^L C_a C_w, \end{aligned} \quad (43)$$

$$\begin{aligned}
H_k(\varepsilon) &\leq \left(\frac{8C_\beta \text{diag}(D \times D) \left(\sum_{\ell=0}^L d_\ell d_{\ell+1} \right) \rho \{ (C_w + C_k) C_\sigma \}^L C_a C_k}{\varepsilon} \right)^{\hat{d}} \\
&\times \log \left(\frac{16 \left(\sum_{\ell=0}^L d_\ell d_{\ell+1} \right) \rho \{ (C_w + C_k) C_\sigma \}^L C_a C_k}{\varepsilon} \right) \\
&\leq \left(\frac{I_k}{\varepsilon} \right)^{\hat{d}+1}, \quad \text{for } 0 < \varepsilon < 2 \left(\sum_{\ell=0}^L d_\ell d_{\ell+1} \right) \rho \{ (C_w + C_k) C_\sigma \}^L C_a C_k,
\end{aligned} \tag{44}$$

where we denoted by

$$\begin{aligned}
I_w &:= 2 \left(\sum_{\ell=0}^L d_\ell d_{\ell+1} \right) \rho \{ (C_w + C_k) C_\sigma \}^L C_a C_w, \\
I_k &:= 8 \max \{ C_\beta \text{diag}(D \times D), 2 \} \left(\sum_{\ell=0}^L d_\ell d_{\ell+1} \right) \rho \{ (C_w + C_k) C_\sigma \}^L C_a C_k.
\end{aligned}$$

By employing (42), (43), and (44), we calculate

$$\begin{aligned}
\int_\alpha^\infty (\log N(\varepsilon, \mathcal{F}_{\mathcal{N}}, \|\cdot\|_S))^{\frac{1}{2}} d\varepsilon &\leq \underbrace{\left(\sum_{\ell=0}^L d_\ell d_{\ell+1} \right)^{\frac{1}{2}} \int_\alpha^\infty (H_w(\varepsilon) + H_k(\varepsilon))^{\frac{1}{2}} d\varepsilon}_{=:(*)} \\
(*) &\leq \int_\alpha^\infty H_w(\varepsilon)^{\frac{1}{2}} d\varepsilon + \int_\alpha^\infty H_k(\varepsilon)^{\frac{1}{2}} d\varepsilon \\
&\leq \int_\alpha^{2(\sum_{\ell=0}^L d_\ell d_{\ell+1}) \rho \{ (C_w + C_k) C_\sigma \}^L C_a C_w} \left(\frac{I_w}{\varepsilon} \right)^{\frac{\hat{d}+1}{2}} d\varepsilon \\
&\quad + \int_\alpha^{2(\sum_{\ell=0}^L d_\ell d_{\ell+1}) \rho \{ (C_w + C_k) C_\sigma \}^L C_a C_k} \left(\frac{I_k}{\varepsilon} \right)^{\frac{\hat{d}+1}{2}} d\varepsilon \\
&\leq \left(\frac{\hat{d}+1}{I_w^{\frac{\hat{d}+1}{2}} + I_k^{\frac{\hat{d}+1}{2}}} \right) \frac{2}{\hat{d}-1} \alpha^{-\frac{\hat{d}-1}{2}} \\
&\leq \frac{4}{\hat{d}-1} \left(\max [2C_w, 8C_k \max \{ C_\beta \text{diag}(D \times D), 2 \}] \left(\sum_{\ell=0}^L d_\ell d_{\ell+1} \right) \rho \{ (C_w + C_k) C_\sigma \}^L C_a \right)^{\frac{\hat{d}+1}{2}} \alpha^{-\frac{\hat{d}-1}{2}},
\end{aligned}$$

that is, we have by (i) of Assumption 4.3.

$$\begin{aligned}
&\int_\alpha^\infty (\log N(\varepsilon, \mathcal{F}_{\mathcal{N}}, \|\cdot\|_S))^{\frac{1}{2}} d\varepsilon \\
&\leq \underbrace{\frac{4}{\hat{d}-1} \left(\max [2C_w, 8C_k \max \{ C_\beta \text{diag}(D \times D), 2 \}] (LC_d^2)^{\frac{\hat{d}+2}{\hat{d}+1}} \rho \{ (C_w + C_k) C_\sigma \}^L C_a \right)^{\frac{\hat{d}+1}{2}}}_{=:K} \alpha^{-\frac{\hat{d}-1}{2}}
\end{aligned}$$

which implies that we conclude that with (31)

$$\begin{aligned}\mathfrak{R}_S(\mathcal{F}_{\mathcal{N}}) &\leq 4 \inf_{\alpha \geq 0} \left\{ \alpha + \frac{3K}{\sqrt[n]{n}} \alpha^{-\frac{\hat{d}-1}{2}} \right\} \\ &= 4 \left(\left(\frac{(\hat{d}-1)K'}{2} \right)^{\frac{2}{\hat{d}+1}} + K' \left(\frac{(\hat{d}-1)K'}{2} \right)^{\frac{2}{\hat{d}+1} \left(-\frac{\hat{d}-1}{2} \right)} \right) = \gamma L^{\frac{\hat{d}+2}{\hat{d}+1}} \{(C_w + C_k)C_\sigma\}^L \left(\frac{1}{n} \right)^{\frac{1}{\hat{d}+1}}\end{aligned}$$

where γ is the positive constant defined by

$$\gamma := 4 \left\{ \left(\frac{\hat{d}-1}{2} \right)^{\frac{2}{\hat{d}+1}} + \left(\frac{\hat{d}-1}{2} \right)^{-\frac{\hat{d}-1}{\hat{d}+1}} \right\} \left(\frac{12}{\hat{d}-1} \right)^{\frac{2}{\hat{d}+1}} \quad (45)$$

$$\times \max[2C_w, 8C_k \max\{C_\beta \text{diag}(D \times D), 2\}] C_d^{\frac{2(\hat{d}+2)}{\hat{d}+1}} \rho C_a.$$

□

F Proof of Theorem 4.6

Theorem F.1 (Theorem 4.6). *Let Assumptions 4.1 and 4.5 hold. Then,*

$$\mathfrak{R}_S(\mathcal{F}_{\widetilde{\mathcal{N}}}) \leq \tilde{\gamma} L^{\frac{\hat{d}+2}{\hat{d}+1}} (C_w^{M+1} C_\sigma^M C_k)^L \left(\frac{1}{n} \right)^{\frac{1}{\hat{d}+1}}, \quad (46)$$

where $\tilde{\gamma}$ is the positive constant independent of L and n , defined in 59.

Proof. The following argument is almost same with the proof of Theorem 4.4 By employing Theorem 1.1 in Kakade and Tewari [2008], we have

$$\mathfrak{R}_S(\mathcal{F}_{\widetilde{\mathcal{N}}}) \leq \inf_{\alpha \geq 0} \left\{ 4\alpha + \frac{12}{\sqrt{n}} \int_\alpha^\infty (\log N(\varepsilon, \mathcal{F}_{\widetilde{\mathcal{N}}}, \|\cdot\|_S))^{\frac{1}{2}} d\varepsilon \right\} \quad (47)$$

In the following, we will estimate the covering number $N(\varepsilon, \mathcal{F}_{\widetilde{\mathcal{N}}}, \|\cdot\|_S)$.

Let $f = \ell(\mathcal{G}(\cdot), \cdot)$ and $f' = \ell(\mathcal{G}'(\cdot), \cdot)$ where $\mathcal{G}, \mathcal{G}' \in \widetilde{\mathcal{N}}$. By (i) of Assumption 4.1, we calculate

$$|f(a, u) - f'(a, u)| = |\ell(\mathcal{G}(a), u) - \ell(\mathcal{G}'(a), u)| \leq \rho \|\mathcal{G}(a) - \mathcal{G}'(a)\|_{\mathbf{L}^2(D; \mathbb{R}^{d_u})}. \quad (48)$$

Denoting by

$$\begin{aligned}\mathcal{G}_\ell &:= f_\ell \circ \mathcal{K}_\ell \circ f_{\ell-1} \circ \mathcal{K}_{\ell-1} \circ \cdots \circ f_0 \circ \mathcal{K}_0, \\ \mathcal{G}'_\ell &:= f'_\ell \circ \mathcal{K}'_\ell \circ f'_{\ell-1} \circ \mathcal{K}'_{\ell-1} \circ \cdots \circ f'_0 \circ \mathcal{K}'_0,\end{aligned}$$

the quantity $\|\mathcal{G}(a) - \mathcal{G}'(a)\|_{\mathbf{L}^2(D; \mathbb{R}^{d_u})}$ is evaluated by

$$\begin{aligned}
& \|\mathcal{G}(a) - \mathcal{G}'(a)\|_{\mathbf{L}^2(D; \mathbb{R}^{d_u})} = \|\mathcal{G}_L(a) - \mathcal{G}'_L(a)\|_{\mathbf{L}^2(D; \mathbb{R}^{d_{L+1}})} \\
& = \left\| f_L \circ \mathcal{K}_L(\mathcal{G}_{L-1}(a)) - f_L \circ \mathcal{K}_L(\mathcal{G}'_{L-1}(a)) \right. \\
& \quad \left. + f_L \circ \mathcal{K}_L(\mathcal{G}'_{L-1}(a)) - f'_L \circ \mathcal{K}'_L(\mathcal{G}'_{L-1}(a)) \right\|_{\mathbf{L}^2(D; \mathbb{R}^{d_{L+1}})} \\
& \stackrel{\text{Assumption 4.5(v)}}{\leq} \left(\underbrace{\|f_L\|_{\text{op}}}_{\leq C_w^{M+1} C_\sigma^M} \underbrace{\|\mathcal{K}_L\|_{\text{op}}}_{\leq C_k} \right) C_\sigma \|\mathcal{G}_{L-1}(a) - \mathcal{G}'_{L-1}(a)\|_{\mathbf{L}^2(D; \mathbb{R}^{d_L})} \\
& \quad + \left(\|f_L - f'_L\|_{\text{op}} + \|\mathcal{K}_L - \mathcal{K}'_L\|_{\text{op}} \right) C_\sigma \|\mathcal{G}'_{L-1}(a)\|_{\mathbf{L}^2(D; \mathbb{R}^{d_L})}.
\end{aligned} \tag{49}$$

Here, we have employed the following estimation:

$$\|f_L\|_{\text{op}} = \|W_{L,M} \circ \sigma(W_{L,M-1}) \circ \cdots \circ \sigma(W_{L,1}) \circ \sigma(W_{L,0})\|_{\text{op}} \leq C_w^{M+1} C_\sigma^M, \tag{50}$$

By the same argument in (49)–(50), we evaluate

$$\begin{aligned}
& \|\mathcal{G}_{L-1}(a) - \mathcal{G}'_{L-1}(a)\|_{\mathbf{L}^2(D; \mathbb{R}^{d_L})} \\
& \leq C_w^{M+1} C_k^M C_\sigma \|\mathcal{G}_{L-2}(a) - \mathcal{G}'_{L-2}(a)\|_{\mathbf{L}^2(D; \mathbb{R}^{d_{L-1}})} \\
& \quad + \left(\|f_{L-1} - f'_{L-1}\|_{\text{op}} + \|\mathcal{K}_{L-1} - \mathcal{K}'_{L-1}\|_{\text{op}} \right) C_\sigma \|\mathcal{G}'_{L-2}(a)\|_{\mathbf{L}^2(D; \mathbb{R}^{d_{L-1}})}.
\end{aligned} \tag{51}$$

By repeatedly evaluating $\|\mathcal{G}_\ell(a) - \mathcal{G}'_\ell(a)\|_{\mathbf{L}^2(D; \mathbb{R}^{d_{\ell+1}})}$ ($\ell = L, L-1, \dots, 0$), we obtain

$$\begin{aligned}
& \|\mathcal{G}(a) - \mathcal{G}'(a)\|_{\mathbf{L}^2(D; \mathbb{R}^{d_u})} \\
& \leq (C_w^{M+1} C_\sigma^M C_k)^L \underbrace{\|(f_0 \circ \mathcal{K}_0)(a) - (f'_0 \circ \mathcal{K}'_0)(a)\|_{\mathbf{L}^2(D; \mathbb{R}^{d_1})}}_{\stackrel{\text{Assumption 4.5(iv)}}{\leq C_a(C_k \|f_0 - f'_0\|_{\text{op}} + C_w^{M+1} C_\sigma^M \|\mathcal{K}_0 - \mathcal{K}'_0\|_{\text{op}})}} \\
& \quad + \sum_{\ell=0}^{L-1} \left(\underbrace{C_k \|f_{\ell+1} - f'_{\ell+1}\|_{\text{op}}}_{(54)} + C_w^{M+1} C_\sigma^M \|\mathcal{K}_{\ell+1} - \mathcal{K}'_{\ell+1}\|_{\text{op}} \right) \\
& \quad \times \underbrace{(C_w^{M+1} C_\sigma^M C_k)^{L-1-\ell} \|\mathcal{G}'_\ell(a)\|_{\mathbf{L}^2(D; \mathbb{R}^{d_{\ell+1}})}}_{\stackrel{(53)}{\leq} (C_w^{M+1} C_\sigma^M C_k)^L C_a} \\
& \leq (C_w^{M+1} C_\sigma^M C_k)^L C_a C_w^M C_\sigma^M \sum_{\ell=0}^L \left(\left(\sum_{m=0}^M C_k \|W_{\ell,m} - W'_{\ell,m}\|_{\text{op}} \right) + C_w \|\mathcal{K}_\ell - \mathcal{K}'_\ell\|_{\text{op}} \right)
\end{aligned} \tag{52}$$

Here, we have employed the following estimations:

$$\|\mathcal{G}'_\ell\|_{\mathbf{L}^2(D; \mathbb{R}^{d_{\ell+1}})} \leq (C_w^{M+1} C_\sigma^M C_k)^{\ell+1} C_a. \tag{53}$$

$$\|f_\ell - f'_\ell\|_{\text{op}} \leq C_w^{M+1} C_\sigma^M \sum_{m=0}^M \|W_{\ell,m} - W'_{\ell,m}\|_{\text{F}} \tag{54}$$

Combining (48), (52), (39), and (40), the norm $\|f - f'\|_S$ is estimated by

$$\begin{aligned} \|f - f'\|_S &= \left(\frac{1}{n} \sum_{i=1}^n |f(a_i, u_i) - f'(a_i, u_i)|^2 \right)^{\frac{1}{2}} \\ &\leq \sum_{\ell=0}^L \left[\sum_{m=0}^M \sum_{j=1}^{d_{\ell,m+1}^w} \sum_{i=1}^{d_{\ell,m}^w} \rho(C_w^{M+1} C_\sigma^M C_k)^L C_a C_w^{M+1} C_\sigma^M C_k \left| \frac{w_{\ell,m,ij}}{C_w} - \frac{w'_{\ell,m,ij}}{C_w} \right| \right. \\ &\quad \left. + \sum_{j=1}^{d_\ell^k} \sum_{i=1}^{d_\ell^k} \rho(C_w^{M+1} C_\sigma^M C_k)^L C_a C_w^{M+1} C_\sigma^M C_k \left\| \frac{k_{\ell,ij}}{C_k/|D|} - \frac{k'_{\ell,ij}}{C_k/|D|} \right\|_{\mathbf{L}^\infty(D \times D; \mathbb{R})} \right], \end{aligned}$$

which implies that we have

$$\begin{aligned} &N(\varepsilon, \mathcal{F}_{\mathcal{N}}, \|\cdot\|_S) \\ &\leq \prod_{\ell=0}^L \prod_{j=1}^{d_{\ell+1}} \prod_{m=0}^M \prod_{j=1}^{d_{\ell,m+1}^w} \prod_{i=1}^{d_{\ell,m}^w} \prod_{j'=1}^{d_{\ell+1}^k} \prod_{i'=1}^{d_\ell^k} \\ &\quad \times N \left(\frac{\varepsilon}{2 \left(\sum_{\ell=0}^L \sum_{m=0}^M d_{\ell,m+1}^w d_{\ell,m}^w \right) \rho(C_w^{M+1} C_\sigma^M C_k)^L C_a C_w^{M+1} C_\sigma^M C_k}, [-1, 1], |\cdot| \right) \\ &\quad \times N \left(\frac{\varepsilon}{2 \left(\sum_{\ell=0}^L d_{\ell+1}^k d_\ell^k \right) \rho(C_w^{M+1} C_\sigma^M C_k)^L C_a C_w^{M+1} C_\sigma^M C_k}, \mathcal{F}_{C_\beta}, \|\cdot\|_{\mathbf{L}^\infty(D \times D; \mathbb{R})} \right), \end{aligned} \tag{55}$$

By taking logarithmic functions in (55), we have

$$\begin{aligned} &\log N(\varepsilon, \mathcal{F}_{\mathcal{N}}, \|\cdot\|_S) \\ &\leq \left(\sum_{\ell=0}^L \sum_{m=0}^M d_{\ell,m+1}^w d_{\ell,m}^w d_{\ell+1}^k d_\ell^k \right) \\ &\quad \times \underbrace{\left\{ \log N \left(\frac{\varepsilon}{2 \left(\sum_{\ell=0}^L \sum_{m=0}^M d_{\ell,m+1}^w d_{\ell,m}^w \right) \rho(C_w^{M+1} C_\sigma^M C_k)^L C_a C_w^{M+1} C_\sigma^M C_k}, [-1, 1], |\cdot| \right) \right\}}_{=:\tilde{H}_w(\varepsilon)} \\ &\quad + \underbrace{\left\{ \log N \left(\frac{\varepsilon}{2 \left(\sum_{\ell=0}^L d_{\ell+1}^k d_\ell^k \right) \rho(C_w^{M+1} C_\sigma^M C_k)^L C_a C_w^{M+1} C_\sigma^M C_k}, \mathcal{F}_{C_\beta}, \|\cdot\|_{\mathbf{L}^\infty(D \times D; \mathbb{R})} \right) \right\}}_{=:\tilde{H}_k(\varepsilon)}. \end{aligned} \tag{56}$$

By same arguments in (43) and (44) (using Example 5.3 of Wainwright [2019] and Lemma 4.2 of Gottlieb et al. [2016]), we can estimate \tilde{H}_w and \tilde{H}_k , respectively as follows:

$$\begin{aligned} \tilde{H}_w(\varepsilon) &\leq \left(\frac{\tilde{I}_w}{\varepsilon} \right)^{\hat{d}+1}, \\ &\text{for } 0 < \varepsilon < 2 \left(\sum_{\ell=0}^L \sum_{m=0}^M d_{\ell,m+1}^w d_{\ell,m}^w \right) \rho(C_w^{M+1} C_\sigma^M C_k)^L C_a C_w^{M+1} C_\sigma^M C_k, \end{aligned} \tag{57}$$

$$\begin{aligned} \tilde{H}_k(\varepsilon) &\leq \left(\frac{\tilde{I}_k}{\varepsilon}\right)^{\hat{d}+1}, \\ \text{for } 0 < \varepsilon < 2 \left(\sum_{\ell=0}^L d_{\ell+1}^k d_\ell^k\right) \rho(C_w^{M+1} C_\sigma^M C_k)^L C_a C_w^{M+1} C_\sigma^M C_k, \end{aligned} \quad (58)$$

where we denoted by

$$\begin{aligned} \tilde{I}_w &:= 2 \left(\sum_{\ell=0}^L \sum_{m=0}^M d_{\ell,m+1}^w d_{\ell,m}^w\right) \rho(C_w^{M+1} C_\sigma^M C_k)^L C_a C_w^{M+1} C_\sigma^M C_k, \\ \tilde{I}_k &:= 8 \max\{C_\beta \text{diag}(D \times D), 2\} \left(\sum_{\ell=0}^L d_{\ell+1}^k d_\ell^k\right) \rho(C_w^{M+1} C_\sigma^M C_k)^L C_a C_w^{M+1} C_\sigma^M C_k, \end{aligned}$$

By employing (56), (57), and (58), we calculate

$$\begin{aligned} \int_\alpha^\infty (\log N(\varepsilon, \mathcal{F}_{\mathcal{N}}, \|\cdot\|_S))^{\frac{1}{2}} d\varepsilon &\leq \left(\sum_{\ell=0}^L \sum_{m=0}^M d_{\ell,m+1}^w d_{\ell,m}^w d_{\ell+1}^k d_\ell^k\right)^{\frac{1}{2}} \underbrace{\int_\alpha^\infty (\tilde{H}_w(\varepsilon) + \tilde{H}_k(\varepsilon))^{\frac{1}{2}} d\varepsilon}_{=:(*)} \\ (*) &\leq \int_\alpha^\infty \tilde{H}_w(\varepsilon)^{\frac{1}{2}} d\varepsilon + \int_\alpha^\infty \tilde{H}_k(\varepsilon)^{\frac{1}{2}} d\varepsilon \\ &\leq \int_\alpha^{2(\sum_{\ell=0}^L \sum_{m=0}^M d_{\ell,m+1}^w d_{\ell,m}^w) \rho(C_w^{M+1} C_\sigma^M C_k)^L C_a C_w^{M+1} C_\sigma^M C_k} \left(\frac{\tilde{I}_w}{\varepsilon}\right)^{\frac{\hat{d}+1}{2}} d\varepsilon \\ &\quad + \int_\alpha^{2(\sum_{\ell=0}^L d_{\ell+1}^k d_\ell^k) \rho(C_w^{M+1} C_\sigma^M C_k)^L C_a C_w^{M+1} C_\sigma^M C_k} \left(\frac{\tilde{I}_k}{\varepsilon}\right)^{\frac{\hat{d}+1}{2}} d\varepsilon \\ &\leq \left(\frac{\tilde{I}_w^{\frac{\hat{d}+1}{2}}}{\hat{d}-1} + \frac{\tilde{I}_k^{\frac{\hat{d}+1}{2}}}{\hat{d}-1}\right) \frac{2}{\hat{d}-1} \alpha^{-\frac{\hat{d}-1}{2}} \\ &\leq \frac{4}{\hat{d}-1} \left(\max[2, 8C_k \max\{C_\beta \text{diag}(D \times D), 2\}] LMC_d^2 \right. \\ &\quad \left. \times \rho(C_w^{M+1} C_\sigma^M C_k)^L C_a C_w^{M+1} C_\sigma^M C_k\right)^{\frac{\hat{d}+1}{2}} \alpha^{-\frac{\hat{d}-1}{2}}, \end{aligned}$$

that is, we have by (iii) of Assumption 4.3,

$$\int_\alpha^\infty (\log N(\varepsilon, \mathcal{F}_{\mathcal{N}}, \|\cdot\|_S))^{\frac{1}{2}} d\varepsilon \leq \tilde{K} \alpha^{-\frac{\hat{d}-1}{2}}$$

where

$$\begin{aligned} \tilde{K} &:= \frac{4}{\hat{d}-1} \left(\max[2, 8C_k \max\{C_\beta \text{diag}(D \times D), 2\}] (LMC_d^4)^{\frac{\hat{d}+2}{\hat{d}+1}} \right. \\ &\quad \left. \times \rho(C_w^{M+1} C_\sigma^M C_k)^L C_a C_w^{M+1} C_\sigma^M C_k\right)^{\frac{\hat{d}+1}{2}}, \end{aligned}$$

which implies that we conclude that with (47)

$$\begin{aligned}\mathfrak{R}_S(\mathcal{F}_{\mathcal{N}}) &\leq 4 \inf_{\alpha \geq 0} \left\{ \alpha + \underbrace{\frac{3\tilde{K}}{\sqrt{n}}}_{=: \tilde{K}'} \alpha^{-\frac{\hat{d}-1}{2}} \right\} \\ &= 4 \left(\left(\frac{(\hat{d}-1)\tilde{K}'}{2} \right)^{\frac{2}{\hat{d}+1}} + \tilde{K}' \left(\frac{(\hat{d}-1)\tilde{K}'}{2} \right)^{\frac{2}{\hat{d}+1} \left(-\frac{\hat{d}-1}{2} \right)} \right) = \tilde{\gamma} L^{\frac{\hat{d}+2}{\hat{d}+1}} (C_w^{M+1} C_\sigma^M C_k)^L \left(\frac{1}{n} \right)^{\frac{1}{\hat{d}+1}}\end{aligned}$$

where $\tilde{\gamma}$ is the positive constant defined by

$$\begin{aligned}\tilde{\gamma} := 4 \left\{ \left(\frac{\hat{d}-1}{2} \right)^{\frac{2}{\hat{d}+1}} + \left(\frac{\hat{d}-1}{2} \right)^{-\frac{\hat{d}-1}{\hat{d}+1}} \right\} \left(\frac{12}{\hat{d}-1} \right)^{\frac{2}{\hat{d}+1}} \\ \times \max[2, 8C_k \max\{C_\beta \text{diag}(D \times D), 2\}] (C_d^4 M)^{\frac{\hat{d}+2}{\hat{d}+1}} \rho C_a C_w^{M+1} C_\sigma^M C_k\end{aligned}\tag{59}$$

□

G Proof of Corollary 4.7 and 4.8

Corollary G.1 (Corollary 4.7). *Let Assumptions 4.1 and 4.3 hold. Then, for any $\delta > \log 2$ and $\mathcal{G} \in \mathcal{N}$, the following inequality holds, with probability greater than $1 - 2\exp(-\delta)$:*

$$\mathcal{L}(\mathcal{G}) - \hat{\mathcal{L}}_S(\mathcal{G}) \leq 2\gamma L^{\frac{\hat{d}+2}{\hat{d}+1}} \{(C_w + C_k)C_\sigma\}^L \left(\frac{1}{n} \right)^{\frac{1}{\hat{d}+1}} + (\rho(C_w + C_k)^{L+1} C_\sigma^L C_a + R_u) \sqrt{\frac{2\delta}{n}}.\tag{60}$$

Proof. By using Assumption 4.3, we estimate for $\mathcal{G} \in \mathcal{N}$ and $a \in \text{supp}(\mu_a)$,

$$\begin{aligned}\|\mathcal{G}(a)\|_{\mathbf{L}^2(D; \mathbb{R}^{d_u})} &= \|(W_L + \mathbf{K}_L) \circ \sigma(W_{L-1} + \mathbf{K}_{L-1}) \circ \cdots \circ \sigma(W_0 + \mathbf{K}_0)(a)\|_{\mathbf{L}^2(D; \mathbb{R}^{d_u})} \\ &\leq (C_w + C_k)^{L+1} C_\sigma^L C_a.\end{aligned}$$

Then, by applying Lemma 4.2 as $R = (C_w + C_k)^{L+1} C_\sigma^L C_a$, and combining with Theorem 4.4, we conclude that the inequality (60). □

Corollary G.2 (corollary 4.8). *Let Assumptions 4.1 and 4.5 hold. Then, for any $\delta > \log 2$ and $\mathcal{G} \in \widetilde{\mathcal{N}}$, the following inequality with probability greater than $1 - 2\exp(-\delta)$:*

$$\mathcal{L}(\mathcal{G}) - \hat{\mathcal{L}}_S(\mathcal{G}) \leq 2\tilde{\gamma} L^{\frac{\hat{d}+2}{\hat{d}+1}} (C_w^{M+1} C_\sigma^M C_k)^L \left(\frac{1}{n} \right)^{\frac{1}{\hat{d}+1}} + (\rho(C_w^{M+1} C_\sigma^M C_k)^{L+1} C_a + R_u) \sqrt{\frac{2\delta}{n}}.\tag{61}$$

Proof. By using Assumption 4.5, we estimate for $\mathcal{G} \in \widetilde{\mathcal{N}}$ and $a \in \text{supp}(\mu_a)$,

$$\begin{aligned}\|\mathcal{G}(a)\|_{\mathbf{L}^2(D; \mathbb{R}^{d_u})} &= \|f_L \circ \mathbf{K}_L \circ f_{L-1} \circ \mathbf{K}_{L-1} \circ \cdots \circ f_0 \circ \mathbf{K}_0(a)\|_{\mathbf{L}^2(D; \mathbb{R}^{d_u})} \\ &\leq (C_w^{M+1} C_\sigma^M C_k)^{L+1} C_a.\end{aligned}$$

Then, by applying Lemma 4.2 as $R = (C_w^{M+1} C_\sigma^M C_k)^{L+1} C_a$ and combining with Theorem 4.6, we conclude that the inequality (61). □